

Burrowing fauna mediate alternative stable states in the redox cycling of salt marsh sediments

van de Velde, Sebastiaan J.; Hidalgo-Martinez, Silvia; Callebaut, Ine; Antler, Gilad; James, Rebecca K.; Leermakers, Martine; Meysman, Filip J.R.

DOI

[10.1016/j.gca.2020.02.021](https://doi.org/10.1016/j.gca.2020.02.021)

Publication date

2020

Document Version

Accepted author manuscript

Published in

Geochimica et Cosmochimica Acta

Citation (APA)

van de Velde, S. J., Hidalgo-Martinez, S., Callebaut, I., Antler, G., James, R. K., Leermakers, M., & Meysman, F. J. R. (2020). Burrowing fauna mediate alternative stable states in the redox cycling of salt marsh sediments. *Geochimica et Cosmochimica Acta*, 276, 31-49. <https://doi.org/10.1016/j.gca.2020.02.021>

Important note

To cite this publication, please use the final published version (if applicable).
Please check the document version above.

Copyright

Other than for strictly personal use, it is not permitted to download, forward or distribute the text or part of it, without the consent of the author(s) and/or copyright holder(s), unless the work is under an open content license such as Creative Commons.

Takedown policy

Please contact us and provide details if you believe this document breaches copyrights.
We will remove access to the work immediately and investigate your claim.

Burrowing fauna mediate alternative stable states in the redox cycling of salt marsh sediments

Sebastiaan J. van de Velde ^{1,2#}, Silvia Hidalgo-Martinez ³, Ine Callebaut ², Gilad Antler ^{4,5},
Rebecca K. James ⁶, Martine Leermakers ², Filip J. R. Meysman ^{3,7}

¹ Department of Earth and Planetary Sciences, University of California, Riverside, CA 92521, USA

² Analytical, Environmental and Geo-Chemistry, Vrije Universiteit Brussel, 1050 Brussel, Belgium

³ Department of Biology, Universiteit Antwerpen, 2610 Wilrijk, Belgium

⁴ Department of Geological and Environmental Sciences, Ben-Gurion University of the Negev, Beersheba, Israel

⁵ The Interuniversity Institute for Marine Sciences, Eilat, Israel

⁶ Department of Estuarine and Delta Systems, NIOZ Royal Netherlands Institute for Sea Research and Utrecht University, 4401 NT Yerseke, The Netherlands

⁷ Department of Biotechnology, Delft University of Technology, 2629 HZ Delft, The Netherlands

Corresponding author: sebastiv@ucr.edu

Submitted to: *Geochimica et Cosmochimica Acta*

Keywords: bioturbation, marine sediments, redox cycling, salt marshes, alternative stable states

Version: revised version 4 (17/02/2020)

Word count: Abstract: 215 / Text: 8 547

*NOTICE: this is the author's version of a work that was accepted for publication in *Geochimica et Cosmochimica Acta*. Changes resulting from the publishing process, such as peer review, editing, corrections, structural formatting, and other quality control mechanisms may not be reflected in this document. Changes may have been made to this work since it was submitted for publication.*

The final publication is available at Elsevier via <https://doi.org/10.1016/j.gca.2020.02.021>

1 **ABSTRACT**

2 The East Anglian salt marsh system (UK) has recently generated intriguing data with respect
3 to sediment biogeochemistry. Neighbouring ponds in these salt marshes show two distinct
4 regimes of redox cycling: the sediments are either iron-rich and bioturbated, or they are
5 sulphide-rich and unbioturbated. No conclusive explanation has yet been given for this
6 remarkable spatial co-occurrence. Here, we quantify the geochemical cycling in both pond
7 types, using pore-water analyses and solid-phase speciation. Our results demonstrate that
8 differences in solid-phase carbon and iron inputs are likely small between pond types, and so
9 these cannot act as the direct driver of the observed redox dichotomy. Instead, our results
10 suggest that the presence of bioturbation plays a key role in the transition from sulphur-
11 dominated to iron-dominated sediments. The presence of burrowing fauna in marine sediments
12 stimulates the mineralisation of organic matter, increases the iron cycling and limits the build-
13 up of free sulphide. Overall, we propose that the observed dichotomy in pond geochemistry is
14 due to alternative stable states, which result from non-linear interactions in the sedimentary iron
15 and sulphur cycles that are amplified by bioturbation. This way, small differences in solid phase
16 input can result in very different regimes of redox cycling due to positive feedbacks. This non-
17 linearity in the iron and sulphur cycling could be an inherent feature of marine sediments, and
18 hence, alternative stable states could be present in other systems.

19 1. INTRODUCTION

20 Most of the present day seafloor is inhabited by burrowing macrofauna (polychaetes,
21 crustaceans, bivalves, etc.), that are considered ecosystem engineers, as they strongly alter the
22 physical and chemical environment in which they live (Jones et al., 1994; Meysman et al. 2006).
23 Benthic fauna affect the redox cycling of carbon, oxygen, iron, sulphur and other elements via
24 feeding behaviour as well as burrow construction and movement (Aller, 1977; Aller and Aller,
25 1998; Meysman et al., 2006; Kristensen et al., 2012; van de Velde et al., 2018). They stimulate
26 transport in the sediment by mixing of solid-phase particles (bio-mixing) and promote the
27 exchange of pore-water solutes with the overlying water column (bio-irrigation). Bio-mixing
28 and bio-irrigation are both lumped under the umbrella term 'bioturbation' (Kristensen et al.,
29 2012) but have distinct effects on organic carbon mineralisation and early diagenesis (Kostka
30 and Luther, 1994; Kostka et al., 2002; van de Velde and Meysman, 2016). Bio-irrigation
31 stimulates aerobic respiration by introducing oxygen into deeper anoxic horizons (Archer and
32 Devol, 1992), and it increases the efflux of reduced Fe^{2+} and H_2S from the sediment, thereby
33 reducing recycling of Fe and S (Elrod et al., 2004; van de Velde and Meysman, 2016; Thibault
34 de Chanvalon et al., 2017). Bio-mixing has an opposite effect; it transports organic matter past
35 the oxic zone, thus decreasing aerobic respiration (Berner and Westrich, 1985), while at the
36 same time, it increases the re-oxidation of iron sulphide minerals, and hence stimulates Fe and
37 S recycling (Swider and Mackin, 1989; Canfield et al., 1993).

38 Recently, salt marshes along the North Sea coast of Norfolk (UK) have been found to host
39 ponds that are either bioturbated or unbioturbated (Mills et al., 2016; Antler et al., 2019;
40 Hutchings et al., 2019). Both pond types host oxygenated waters, but show distinct sediment
41 geochemistries, which appears to belong to two redox end-members. In one type of pond, the
42 sediments are heavily bioturbated and iron rich, while the sediments in a second type of pond
43 do not have burrowing fauna and are sulphide rich. These two different redox states can be
44 found in neighbouring ponds, less than five meters apart, which suggests that local boundary
45 conditions are highly similar (Antler et al., 2019; Hutchings et al., 2019). These salt marsh pond
46 sediments hence provide a unique environment to study the impact of bioturbation on sediment
47 geochemistry, as they allow the effect of burrowing fauna to be quantified by comparing the
48 geochemistry of the two oxygenated ponds.

49 The objective of this study is to better understand the differential geochemical cycling in the
50 ponds of the East Anglian salt marsh system and to investigate the particular role of
51 bioturbation. Recently, Antler et al. (2019) reported pore-water data, as well as carbon, sulphur
52 and oxygen isotope data from the pond sediments, that clearly substantiate the redox dichotomy

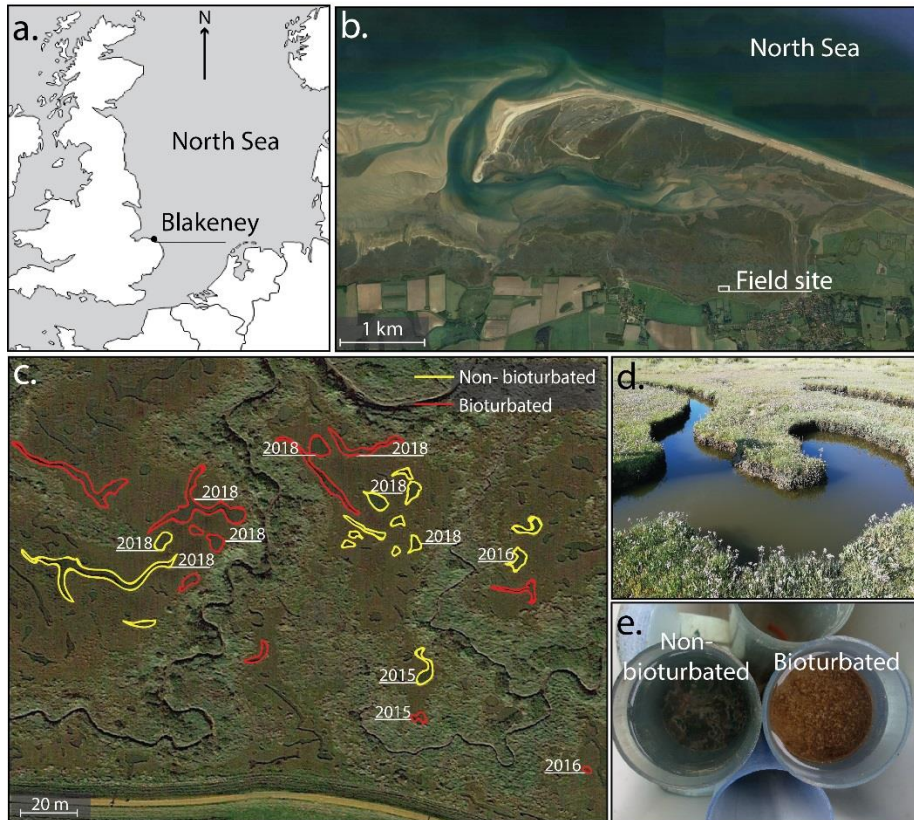
53 and found that the redox state of a given pond remains stable over many years. Hutchings et al.
54 (2019) presented a spatial survey of the East Anglian salt marsh system, and they proposed that
55 the pond distribution could be partially controlled by differences in organic carbon or iron
56 delivery. Here, we present new pore-water and solid-phase data from the East Anglian salt
57 marsh ponds that were collected during three separate visits (in October 2015, August 2016 and
58 August 2018). From these, we put forward a conceptual model that can explain the observed
59 dichotomy in sediment biogeochemistry. The model suggests that the sediments exhibit
60 alternative stable states and that bioturbation plays a crucial role in the formation of these
61 alternative stable states.

62 **2. MATERIALS & METHODS**

63 **2.1 Field site location**

64 The Blakeney salt marsh (Fig. 1a-c; 52° 57' N, 01° 00' E) is part of a larger salt marsh
65 complex that stretches for > 200 km along the North Sea coast of East Anglia (UK), and which
66 was formed some hundreds years ago (Pethick, 1980; Funnell and Pearson, 1989). The higher
67 marsh is vegetated, but contains several shallow, water-filled ponds, which have a surface area
68 ~50 - 500 m² and a water depth of 10 – 20 cm (Fig. 1d,e). These ponds likely formed during
69 the initial stage of marsh development from unvegetated patches (Pye et al., 1990) that were
70 not stabilised by plant roots, and hence were more susceptible to erosion. Over time, these bare
71 patches became depressions that subsequently evolved into ponds (Pethick, 1974).

72 The ponds in Blakeney salt marsh show a clear dichotomy in terms of their sediment
73 geochemistry (Antler et al., 2019; Hutchings et al., 2019). Ponds are either bioturbated and iron-
74 rich, or unbioturbated and sulphide-rich. Moreover, these two redox regimes are so divergent
75 that they can be distinguished by visual inspection of the sediment surface (Antler et al., 2019;
76 Hutchings et al., 2019). The sediment surface of the bioturbated ponds shows a bright reddish
77 colour, most likely originating from high concentrations of iron oxides, and is intersected with
78 *Nereis sp.* worm burrows (Figure 1e, estimated density ~1000 individuals m⁻²; Antler et al.,
79 2019). The sediments of the unbioturbated ponds are black (suggesting high concentrations of
80 iron sulphides) and are often colonised by white mats of large sulphur oxidising bacteria (e.g.
81 *Beggiatoa*) (Fig. 1e).



82

83 **Figure 1:** (a) Geographical location of the Blakeney Salt marsh along the Norfolk coast (UK). (b,c) Overview of the sampling
 84 locations. Aerial picture of the field site, with an indication of the unbioturbated (yellow outlining) and bioturbated (red
 85 outlining) ponds, based on visual inspection of sediment surface. The year annotation denotes the campaigns when the ponds
 86 were sampled (coordinates are given in Table 1). (d) Picture of a typical pond. (e) Pictures of the typical sediment surface of a
 87 bioturbated (reddish with worm burrows) and an unbioturbated (dark sediment covered with microbial mats) pond.

88 2.2 Sampling campaigns

89 Pond water samples and sediment cores were collected on three separate occasions (2015,
 90 2016 and 2018). Twelve ponds were examined in total (sampling sites in Fig. 1c, coordinates
 91 in Table 1). During the first and second campaigns, one bioturbated pond and one unbioturbated
 92 pond were investigated. During the third campaign, four ponds from each type were sampled.
 93 In all three campaigns, the temperature (T), salinity (S) and oxygen (O₂) of the overlying water
 94 were recorded *in situ* using a portable MultiLine Multi 3430 IDS sensor (WTW, Germany).
 95 Additionally, pond water was collected for analysis of soluble reactive phosphorus (SRP),
 96 ammonium (NH₄⁺), dissolved metals (dFe, dMn), dissolved inorganic carbon (DIC) and
 97 sulphate (SO₄²⁻). In 2018, we conducted a small survey to map the spatial pond type distribution
 98 at the field site (Fig. 1c). Ponds were classified based on visual inspection at the sediment-water
 99 interface (sediment coloration and evidence of bioturbation; Fig. 1e) and the presence of
 100 dissolved sulphide in the pore water. The presence of sulphide was tested by inserting a silver
 101 wire in the sediment for 10 minutes. If the wire turned black, this indicated that Ag₂S had
 102 formed, and that the pore water contained high amounts of dissolved sulphide. If there was no

103 colour change, the pore water did not contain high levels of dissolved sulphide (Fig. A1,
 104 Appendix 4). The results of the silver wire assessment were always identical to the visual
 105 inspection of the sediment surface, suggesting that our pond classification procedure was
 106 consistent and robust.

107 **Table 1:** Coordinates and type of the ponds sampled in the 2015, 2016 and 2018 field campaigns in the Blakeney salt marsh
 108 with indication of analyses done on core samples (see main text for details). See Fig. 1c for relative geographical location of
 109 the ponds.

	Coordinates		Type	Year sampled	Core analyses	
					Pore water	Solid Phase
1	52° 57' 22.7'' N	01° 00' 14.0'' E	Bioturbated	2015	dFe, dMn, SO ₄ ²⁻ , Cl ⁻ , NH ₄ ⁺ , ΣH ₂ S	porosity, grain size, POC, TN, ²¹⁰ Pb, ¹³⁷ Cs, Fe speciation, S speciation
2	52° 57' 23.0'' N	01° 00' 14.0'' E	Unbioturbated	2015	"	"
3	52° 57' 22.2'' N	01° 00' 16.6'' E	Bioturbated	2016	"	porosity, POC, TN, Fe speciation, S speciation
4	52° 57' 24.0'' N	01° 00' 16.0'' E	Unbioturbated	2016	"	"
5	52° 57' 25.2'' N	01° 00' 13.2'' E	Bioturbated	2018	-	porosity, grain size, POC, TN
6	52° 57' 25.3'' N	01° 00' 12.5'' E	Bioturbated	2018	-	"
7	52° 57' 24.6'' N	01° 00' 10.6'' E	Bioturbated	2018	-	"
8	52° 57' 24.3'' N	01° 00' 10.9'' E	Bioturbated	2018	-	"
9	52° 57' 24.7'' N	01° 00' 13.4'' E	Unbioturbated	2018	-	"
10	52° 57' 24.4'' N	01° 00' 14.1'' E	Unbioturbated	2018	-	"
11	52° 57' 24.3'' N	01° 00' 9.9'' E	Unbioturbated	2018	-	"
12	52° 57' 24.1'' N	01° 00' 10.1'' E	Unbioturbated	2018	-	"

110
 111 During the 2015 campaign, 4 sediment cores were collected from each pond by manual
 112 insertion of transparent PVC core liners (6 cm inner diameter; 30 cm long). During retrieval
 113 and transport to the nearby field laboratory (~2 km away), care was taken to avoid disturbance
 114 of the sediment. To verify the integrity of our extraction procedure, pore water was collected in
 115 two alternative ways. In 2 replicate cores from each pond, pore water was extracted using
 116 rhizons within ~2h of sampling. Rhizons (pore size ~0.1 µm) were placed in predrilled holes
 117 along the length of the sediment core (replicate one: 1 cm intervals over 20 cm, replicate two:
 118 2 cm intervals over 30 cm), and, subsequently, syringes were attached to the rhizons and
 119 manually withdrawn to create a vacuum and extract pore water (Fig. A2, Appendix 4). After 1
 120 hour, syringes were detached, and the retrieved pore water was distributed into sampling vials
 121 without filtration (depending on the analyte, a fixative was added – see section 2.4). The
 122 remaining 2 replicate cores were left overnight in an incubation tank filled with water collected
 123 from the sampling site. The incubation tank was located in a climate-controlled room at *in-situ*
 124 temperature and bubbled with air to retain 100% air saturated oxygen levels. The next day, the
 125 two cores were sectioned for pore-water extraction in an anaerobic glove box (N₂ atmosphere;
 126 Coy lab products, USA). Slicing was carried out at 0.5 cm intervals from 0 to 3 cm depth, at 1

127 cm intervals between 3 and 8 cm depth, and in 2 cm slices from 8 to 22 cm depth. Sediment
128 sections were collected in 50 mL centrifuge tubes (polypropylene; TPP, Switzerland) and
129 centrifuged at 2500g for 10 min (Sigma 3-18KS, Sigma Laborzentrifugen GmbH, Germany).
130 Subsequently, the centrifuge tubes were opened in the glove box, pore water was filtered
131 through 0.42 μm cellulose acetate filters (Chromafil Xtra) and distributed into sampling vials
132 (depending on the analyte, a fixative was added – see section 2.4). The solid phase that remained
133 after centrifugation was freeze-dried and stored in an aluminium bag under nitrogen atmosphere
134 for solid-phase analyses and radionuclide measurements.

135 During the 2016 campaign, pore-water retrieval was largely similar to the first campaign,
136 with the difference that core sectioning took place immediately after core collection. Pore water
137 was retrieved by rhizons in 2 replicates cores, while the other two cores were sliced in a portable
138 glove bag filled with N_2 -gas (Captair Field Pyramid, Erlab, France) within 2 h after core
139 collection. The oxygen level in the glove bag was continuously monitored (Teledyne 3110
140 equipped with a trace oxygen sensor). Core sectioning and processing was as in the first
141 campaign.

142 Pore-water samples from the first two campaigns were analysed for metals (dFe, dMn),
143 anions (SO_4^{2-} , Cl^-), ammonium (NH_4^+) and total free sulphide ($\Sigma\text{H}_2\text{S} = [\text{H}_2\text{S}] + [\text{HS}^-]$). Cations
144 and anions were always analysed from the pore water extracted via core slicing. To avoid loss
145 of gaseous H_2S upon exposure of pore water to the atmosphere, $\Sigma\text{H}_2\text{S}$ was always analysed
146 from the pore water obtained through rhizons and stabilised with ZnAc (see section 2.4). In
147 2015, NH_4^+ was analysed on the rhizon samples, while in 2016 it was analysed on the
148 centrifugated pore water.

149 During the 2018 campaign, two cores for solid-phase analyses were collected from each
150 investigated pond. Cores were immediately sliced in open air in the field, and no pore water
151 was collected. Sediment samples were transferred to 50 ml centrifuge tubes (polypropylene;
152 TPP, Switzerland) and transported to the University of Antwerp (transit time ~ 12 hours), freeze
153 dried and analysed for carbon and nitrogen content as well as sediment grain size distribution.
154 Additionally, plant material from the 7 most common plants on the high marsh (*Suaeda*
155 *maritima*, *Salicornia radicans*, *Spartina anglica*, *Armenia maritima*, *Elytrigia atherica*,
156 *Halimione portulacoides* and *Limonium vulgare*) was collected, oven dried at 70°C and
157 analysed for total carbon, nitrogen and phosphorus content.

158 **2.3 Sediment parameters**

159 Sediment grain size and sorting was determined on sediment slices from four depth horizons
160 (1-1.5 cm, 5-6 cm, 12-14 cm and 20-22 cm) on one core from each pond sampled in 2015 and
161 2018 (5 replicate analyses per pond type). Grain size distribution was determined by laser
162 diffraction (Malvern Mastersizer 2000) after homogenisation and rewetting of freeze-dried
163 sediment (McCave, 1986). Solid-phase density from each depth slice of all cores sampled in
164 2015 and 2016 was determined by adding a known mass of ground, freeze-dried sediment to a
165 100 ml graduated cylinder filled with tap water and recording the volume displacement.
166 Sediment porosity (volume of pore water per total volume of sediment) from each depth slice
167 of all cores sampled in all three of the campaigns (2 replicate depth profiles per pond type;
168 Table 1) was determined from water content and solid-phase density measurements,
169 considering the salt content of the pore water. The water content of the sediment was determined
170 as the difference in weight before and after freeze-drying.

171 **2.4 Bottom-water and pore-water analyses**

172 In 2015, samples for DIC analysis were collected in 5 mL headspace vials, left to overflow
173 and fixed with 10 μL of a saturated HgCl_2 solution. Analysis was done using an AS-C3 analyzer
174 (Apollo SciTech, USA), consisting of an acidification and purging unit in combination with a
175 LICOR-7000 $\text{CO}_2/\text{H}_2\text{O}$ Gas Analyzer (precision 0.3%). Quality assurance was done by regular
176 analysis of Certified Reference Materials (CRM) obtained from the Scripps Institution of
177 Oceanography (Batch 140; Dickson et al., 2003). In 2018, sample collection was identical, but
178 the sampling vials were 12 mL gastight Exetainer vials (Labco). Analysis was done on an
179 elemental analyser (EuroVector Euro EA 3000, precision < 10 %). Prior to analysis, exetainer
180 vials were injected with He to create a 4 mL headspace, acidified with phosphoric acid (100
181 μL , 99 %, Sigma-Aldrich) and then equilibrated on a rotatory shaker for 12 h.

182 Samples (250 μl) for dissolved metal analysis (dFe, dMn) were stabilised with 50 $\mu\text{L}/\text{mL}$
183 bidistilled HNO_3 (65%, suprapure, Merck) and stored at 4°C. Samples collected in 2015 were
184 diluted 50x with a standard matrix solution containing 35 salinity artificial seawater, 2% HNO_3
185 and 0.2 mg L^{-1} Ytterbium as an internal standard (Crompton, 1989). Analysis was done by
186 Inductively Coupled Plasma – Optical Emission Spectroscopy (ICP-OES, ThermoFisher
187 iCAP6500; precision < 2%, Limit of Quantification - LOQ = 0.02 μM for dFe and dMn), which
188 was calibrated using external standard solutions and quality controlled by regular analysis of
189 ICP multi-element IV CRM. Samples collected in 2016 and 2018 were diluted 20x with a 1%
190 HNO_3 solution and analysis was done by High Resolution - Inductively Coupled Plasma – Mass

191 Spectroscopy (HR-ICP-MS, ThermoScientific Element 2, precision < 5%, LOQ = 5 nM for dFe
192 and 1 nM for dMn), which was calibrated using external standard solutions and quality
193 controlled by regular analysis of SLRS-6 and 1640 CRM. Indium (2.5 ppb) containing 2%
194 HNO₃ was injected simultaneously as an internal standard. Note that we employ the operational
195 term ‘dissolved’ iron and manganese (dFe, dMn), as we measured the total concentration of
196 iron and manganese after passage through a 0.42 μm filter, which can contain colloidal or
197 nanoparticulate iron and manganese (with different oxidation states) (Raiswell and Canfield,
198 2012).

199 Samples (250 μL) for SO₄²⁻ and Cl⁻ analyses were fixed with 100μL ZnAc (5%) per mL, to
200 avoid oxidation of free sulphide to sulphate. After 10x dilution, samples were analysed by ion
201 chromatography, using an isocratic eluent (3.5 mM Na₂CO₃ / 1 mM NaHCO₃) combined with
202 a Dionex AS-14 analytical column (Thermo Scientific) and conductivity detection (ED40
203 electrochemical detector) with a precision of 8% and a LOQ of 0.005 mM for both Cl⁻ and SO₄²⁻
204 (Gros et al., 2008). The instrument was calibrated using external standards and quality
205 controlled by regular analysis of a control sample (Quasimeme, QNU 253 ew). Reported SO₄²⁻
206 concentrations were normalised for chloride content (
207 $[SO_4^{2-}]_{corrected} = [SO_4^{2-}]_{measured} / [Cl^-]_{measured} * \overline{[Cl^-]_{measured}}$), to account for salinity gradients that
208 occur in these salt marsh sediments (Mills et al., 2016).

209 Nutrient samples (NH₄⁺, SRP) were diluted 25 times with a low nutrient seawater matrix
210 solution and analysed by a SEAL QuAAtro segmented flow analyser (precision < 4%, LOQ =
211 0.2μM for NH₄⁺ and 0.1 μM for SRP), which was calibrated using external standards and
212 quality controlled by regular interlaboratory comparisons (Aminot et al., 2009).

213 Subsamples (1 ml) for free sulphide analysis were fixed with 100 μL of ZnAc (5%) per mL
214 of sample, and measured spectrophotometrically using the method of Cline (Cline, 1969)
215 (precision not determined).

216 **2.5 Radionuclides**

217 Subsamples of one replicate core from each pond studied in 2015 were analysed for ²¹⁰Pb
218 and ¹³⁷Cs activity at Utrecht University. Samples for ²¹⁰Pb were spiked with ²⁰⁹Po and
219 subsequently microwave digested in 10 mL HCl (concentrated) for 3h. Afterwards, 2 mL 3.5%
220 HClO₄ was added and the mixture was evaporated to remove the acids. The precipitate was
221 then re-dissolved in 5 mL HCl (concentrated) for 30 min. Subsequently, 40 mL of boric acid
222 (12 g L⁻¹ in 0.5M HCl), 4 mL NH₄OH and 5 mL of ascorbic acid (40 g L⁻¹ in 0.5M HCl) were
223 added and Po isotopes were deposited by suspending a silver disk in the solution, which was

224 heated to 80°C for 4h and left overnight. Counting of ^{210}Po was done using a Canberra
225 Passivated Implanted Planar Silicon detector (Canberra Industries, USA), allowing the ^{210}Pb
226 activity to be calculated (precision < 5%). $^{210}\text{Pb}_{\text{excess}}$ was calculated by subtracting the average
227 of ^{214}Pb and ^{214}Bi activity (which represents the ^{210}Pb activity in equilibrium with ^{226}Ra) from
228 the total ^{210}Pb value.

229 The sedimentation flux is the amount of solids that pass through a given sediment horizon
230 (when a coordinate system is tied to the sediment-water interface). If we assume that sediment
231 compaction is in steady state (any changes with depth in porosity are balanced by changes in
232 sedimentation velocity), the sedimentation flux J_s (expressed in $\text{kg m}^{-2} \text{yr}^{-1}$) is constant
233 throughout the whole sediment column (Meysman et al., 2005). The mean sedimentation
234 velocity over a given sediment layer can be calculated as

$$235 \quad v = J_s / ((1 - \phi_{\text{AVG}}) \rho_s) \quad [1]$$

236 where ϕ_{AVG} is the mean porosity in the sediment layer. The Periodic Flux model (PF; Sanchez-
237 Cabeza et al., 2000) was fitted to the $^{210}\text{Pb}_{\text{excess}}$ profile of the unbioturbated core to determine
238 the sedimentation flux and sedimentation velocity. The PF model is a generalisation of the more
239 widely used constant flux model (Appleby and Oldfield, 1978), and is valid when the flux of
240 $^{210}\text{Pb}_{\text{excess}}$ to the sediment is variable. To validate the PF model, we used an independent tracer
241 (^{137}Cs ; Sanchez-Cabeza and Ruiz-Fernández, 2012). The sedimentation flux can be calculated
242 from the ^{137}Cs depth profile according to

$$243 \quad J_s = \frac{\rho_s}{\tau} \int_0^L (1 - \phi(x)) dx \quad [2]$$

244 Where L is the depth of the ^{137}Cs peak and τ is the known time since ^{137}Cs peak input (which
245 was assumed to be the year 1963).

246 The bioturbated core experienced sediment mixing, and hence the PF model could not be
247 applied to the corresponding $^{210}\text{Pb}_{\text{excess}}$ profile. Alternatively, we used the peak depth of the
248 ^{137}Cs depth profile to determine the sedimentation flux (eq. [2]). Furthermore, because our data
249 indicated a highly variable ^{210}Pb flux, the scatter on the data did not allow to constrain a mixing
250 depth or bio-diffusion coefficient from the $^{210}\text{Pb}_{\text{excess}}$ profiles (Lecroart et al., 2010).

251 **2.6 Solid-phase analyses**

252 Freeze-dried samples and oven-dried plant samples were ground to a fine powder and
253 analysed by an Interscience Flash 2000 organic element analyser (precision <5%) for
254 determination of particulate organic carbon (POC) and total nitrogen (TN). Before analysis and

255 after weighing, samples for POC were first acidified with 0.1M HCl to remove the inorganic
256 carbon (Nieuwenhuize et al., 1994). Concentrations of POC are expressed as mass % of dry
257 sediment. The C:N ratio of the organic matter in the sediment was calculated as the ratio of
258 POC over TN ($C_{org}:N_{tot}$).

259 Freeze-dried sediment subsamples (300 mg) from each sediment horizon sampled in 2015
260 and 2016 were used for sequential iron extraction as described by Poulton and Canfield (2005).
261 This extraction determines 4 operational iron phases: (i) carbonate associated iron + acid-
262 volatile sulphide ($Fe_{carb+AVS}$), (ii) easily reducible iron oxides (Fe_{ox1}), (iii) moderately reducible
263 iron oxides (Fe_{ox2}) and (iv) magnetite (Fe_{mag}). Iron associated with sulphide (Fe_{AVS}) and pyrite-
264 iron (Fe_{pyr}) were determined in a separate extraction procedure (as discussed below). The
265 extraction solutions and extraction times are summarised in Table A1 (Appendix 3). At the
266 beginning of each extraction step, 10 mL of extraction solution was added, and the sample was
267 extracted under constant agitation. Subsequently, the sample was centrifuged (2500g for 10
268 min) and the supernatant was filtered (0.45 μ m cellulose acetate) and stored at 4°C for later
269 analysis on ICP-OES (similar procedure as for pore-water samples). The next extraction step
270 was started immediately, and all steps were executed inside a nitrogen-filled glove box.

271 Sediment subsamples (300 mg) from each sediment horizon sampled in 2015 and 2016 were
272 analysed for acid-volatile sulphide (AVS) and chromium reducible sulphide (CRS) with a cold,
273 two-step distillation procedure (Kallmeyer et al., 2004), based on the methods of Canfield et al.
274 (1986) and Cornwell and Morse (1987). Freeze-dried sediment was directly weighed in the
275 distillation flasks, which was immediately purged with N_2 -gas. The first step extracts the AVS
276 fraction via addition of a 6M HCl solution. H_2S is stripped from solution using N_2 as a carrier
277 gas, and subsequently trapped in a 10 mL zinc acetate solution (5 %), with a drop of antifoam.
278 After 40 min., the trap is replaced and 20 mL of N,N di-methyl formamide (DMF) is added to
279 the distillation flask to solubilise the elemental sulphur fraction, followed by 12 mL of a reduced
280 chromium solution (Table A1, Appendix 3). The H_2S released is trapped in an identical way as
281 for the AVS fraction. The sulphide in the ZnAc traps is measured spectrophotometrically using
282 the method of Cline (1969). For subsequent calculations, we assume that AVS consists
283 primarily of iron monosulphide minerals (FeS) (Cornwell and Morse, 1987), and the CRS
284 fraction contains both elemental sulphur (S^0) and pyrite (FeS_2) (Kallmeyer et al., 2004). To
285 determine the elemental sulphur content, 10 mL of methanol was added to a separate subsample
286 (300 mg) and the mixture was left to agitate overnight. Afterwards, the sample was centrifuged
287 and cyclo-octasulphur was measured by ultrahigh pressure liquid chromatography (UPLC)
288 using a Waters Acquity H-class instrument with a Waters column (methanol eluent 0.4 ml min⁻¹

289 ¹, Acquity UPLC BEH C18, 1.7- μ m, 2.1 x 50 mm column; Waters, Japan) and detected by
 290 absorbance at 265 nm on a Waters PDA detector (Kamyshny et al., 2009), using external
 291 standards (reproducibility ~6%). CRS concentrations were corrected for S⁰ content ($S_{pyr} = CRS$
 292 $- S^0$). Similarly, $Fe_{carb+AVS}$ in the iron speciation was corrected for Fe_{AVS} (
 293 $Fe_{carb} = Fe_{carb+AVS} - Fe_{AVS}$, assuming all AVS was FeS). Results of the sulphur speciation are
 294 reported in μ mol g⁻¹ of dry sediment and total inorganic sulphur is calculated as $S_{inorg} = AVS +$
 295 $S^0 + S_{pyr}$. Pyritic iron (Fe_{pyr}) is calculated assuming a stoichiometric ratio of 1:2 Fe:S for the
 296 S_{pyr} fraction. For clarity, iron speciation is reported in % of the total reactive iron fraction (Fe_{reac}
 297 $= Fe_{carb} + Fe_{AVS} + Fe_{ox1} + Fe_{ox2} + Fe_{mag} + Fe_{pyr}$).

298 **2.7 Diffusive fluxes, burial rates and cycling numbers**

299 Diffusive fluxes of dissolved species were calculated based on the pore-water profiles, using
 300 Fick's first law:

$$301 \quad J_{diff} = -\phi \frac{D_0(S,T)}{\theta^2} \frac{\partial C}{\partial x} \quad [3]$$

302 where J_{diff} is the diffusive flux, C is the concentration in the pore water, x is the depth into
 303 the sediment, ϕ represents porosity, and θ^2 is the correction factor for sediment tortuosity (
 304 $\theta^2 = 1 - 2 \ln \phi$) (Boudreau, 1996). The molecular diffusion coefficient (D_0) is calculated based
 305 on salinity and temperature using the R package CRAN:marelac (Soetaert et al., 2010), which
 306 is based on the constitutive relations presented in Boudreau (1997). The concentration gradient,
 307 $\partial C / \partial x$, was calculated by the linear regression from the concentration profiles at specific
 308 depths in the sediment. Sulphide fluxes were calculated from the total free sulphide
 309 concentration gradient but using the diffusion coefficient of HS⁻. Sulphate fluxes were derived
 310 from uncorrected sulphate profiles (thus before rescaling for the Cl⁻ concentration).

311 Burial fluxes of POC, TN, all inorganic sulphide fractions and all reactive iron fractions
 312 were calculated based on the sedimentation flux (J_s) as derived from the radionuclide profiles
 313 and the concentration of the solid component at the bottom of the sediment column (C_{solid}):

$$314 \quad J_{burial} = J_s C_{solid} \quad [4]$$

315 The cycling number, which represents the number of times an element is reduced before
 316 being buried, can be calculated as the ratio of the total reduction rate R_{red}^{tot} over the total burial

317 flux J_{burial} (Canfield et al., 1993)

$$318 \quad N = \frac{R_{red}^{tot}}{J_{burial}} \quad [5]$$

319 **2.8 Statistics**

320 Where reported, the uncertainty (SE) associated with a calculated value x (not derived from
321 direct measurements) are calculated based on the standard propagation of errors. For the
322 statistical analyses, each pond was considered an independent replicate, and duplicate
323 measurements were averaged to get a single value for each pond. Comparisons of POC
324 concentrations and $C_{org}:N_{tot}$ ratios of organic matter were not expected to vary over time, and
325 therefore, measurements from all three sampling campaigns were used in a one-way ANOVA
326 to compare between the bioturbated and unbioturbated pond types ($n = 6$). Comparisons of the
327 nutrient, anion, cation and DIC concentrations for the replicate ponds were also conducted with
328 a one-way ANOVA, using only the measurements from 2018 to avoid seasonal differences (n
329 $= 4$). Residuals were tested for normality and homoscedasticity, and passed these assumptions,
330 and p-values less than 0.05 were considered significant.

331 **3. RESULTS**

332 **3.1 Bottom water conditions**

333 The salinity was similar in the two pond types in each campaign but varied substantially
334 between campaigns (range 24-44; Table 2). This indicates that the ponds experience a similar
335 hydrological regime, consisting of regular flushing with North Sea seawater ($S \sim 34$), combined
336 with the seasonal dynamics of meteoric input and evaporation. In 2015, the water was clear in
337 both pond types, which contrasted with 2016 and 2018, when the water of the unbioturbated
338 ponds was colonised by green macroalgae (Fig. A3, Appendix 4). The sediment surface of the
339 bioturbated ponds showed faecal casts, thus providing visual evidence for the presence of
340 *Arenicola* spp.. During sediment core processing, we found *Nereis* sp. in the bioturbated cores
341 (Fig. A4, Appendix 4), consistent with previous observations (Antler et al., 2019; Hutchings et
342 al., 2019). In 2015, the daytime oxygen level was considerably lower in the unbioturbated (25%
343 air saturation) than in the bioturbated pond (79%). In 2016 and 2018, oxygen was supersaturated
344 in all ponds (Table 2), coincident with the presence of photosynthesizing macroalgae in the
345 unbioturbated ponds. After filtration of bioturbated pond water, filters were distinctly green in
346 colour, likely due to the presence of pelagic microalgae or resuspended microphytobenthos.
347 Nutrient and metal concentrations in the ponds varied between sampling times, but a

348 comparison of replicates from 2018, showed no clear pattern with pond type (Table 2). Sulphate
 349 concentrations mainly varied with salinity. DIC concentrations were higher in the bioturbated
 350 ponds, but this was not statistically significant (One-way ANOVA, $F\text{-value}_{1,6} = 5.167$, $p = 0.06$).

351 **Table 2:** Summary of bottom-water conditions, sediment and salt marsh plant properties for the two different pond types per
 352 sampling time. Errors represent the standard deviation of all measured samples (mean \pm 1 s.d; $n_{(2015 \& 2016)} = 3$, $n_{(2018)} = 12$).
 353 Three measurements were made per pond, Values without standard deviation are from single measurements. *Salinity for the
 354 2015 campaign was derived from the Cl^- content in the overlying water.

Parameter	Symbol	Units	Unbioturbated pond			Bioturbated pond		
			2015	2016	2018	2015	2016	2018
# ponds measured			1	1	4	1	1	4
<i>Bottom water conditions</i>								
Temperature	T	°C	10.0	17.0	26 \pm 2	10.3	19.1	26 \pm 2
Salinity	S	-	31*	27	44 \pm 4	30*	26	43 \pm 2
pH	-	-	7.61 \pm 0.03	7.8 \pm 0.2	8.3 \pm 0.1	7.9 \pm 0.3	7.6 \pm 0.1	8.0 \pm 0.1
Oxygen concentration	-	% air saturation	25	>100	>100	79	>100	>100
DIC concentration	-	mM	3.91 \pm 0.01	NA	4.2 \pm 0.7	4.69 \pm 0.01	NA	5.2 \pm 0.5
NH ₄ ⁺ concentration	-	μM	8.1 \pm 0.5	5.4 \pm 0.4	6 \pm 2	8.0 \pm 0.6	0.6 \pm 0.2	5 \pm 2
SRP concentration	-	μM	0.3 \pm 0.1	0.4 \pm 0.1	2 \pm 1	1.7 \pm 0.1	11.3 \pm 0.4	4 \pm 4
SO ₄ ²⁻ concentration	-	mM	24.3 \pm 0.1	21.9 \pm 0.2	33 \pm 8	22.0 \pm 0.3	19.3 \pm 0.1	32 \pm 9
dFe concentration	-	μM	<LOD	0.16 \pm 0.01	0.9 \pm 0.7	<LOD	0.5 \pm 0.1	0.8 \pm 0.6
dMn concentration	-	μM	<LOD	5.96 \pm 0.03	5 \pm 2	2.4 \pm 0.1	5.7 \pm 0.1	3 \pm 1
<i>Sediment properties (depth-averaged)</i>								
C:N ratio	C _{org} :N _{tot}	-	12 \pm 1	12 \pm 2	13 \pm 1	11 \pm 1	11.9 \pm 0.7	12.8 \pm 0.9
Porosity	φ	-	0.88 \pm 0.06	0.86 \pm 0.07	0.86 \pm 0.04	0.79 \pm 0.09	0.83 \pm 0.07	0.81 \pm 0.06
Solid-phase density	ρ _{solid}	g cm ⁻³	2.2 \pm 0.2	1.6 \pm 0.3	-	2.1 \pm 0.2	2.0 \pm 0.5	-
Sedimentation	v ₀	cm yr ⁻¹	0.3 \pm 0.1	-	-	0.3 \pm 0.1	-	-
sedimentation flux	J _{sed}	g cm ⁻² yr ⁻¹	0.08 \pm 0.02	0.07 \pm 0.03	-	0.13 \pm 0.05	0.10 \pm 0.04	-
<i>Salt marsh plant properties</i>								
		<i>Suaeda maritima</i>	<i>Salicornia radicans</i>	<i>Spartina anglica</i>	<i>Armenia maritima</i>	<i>Elytrigia atherica</i>	<i>Halimione portulacoides</i>	<i>Limonium vulgare</i>
C:N ratio	C _{org} :N _{tot}	18	20	27	20	74	26	25
C:P ratio	C _{org} :P _{tot}	682	492	669	554	1289	802	692

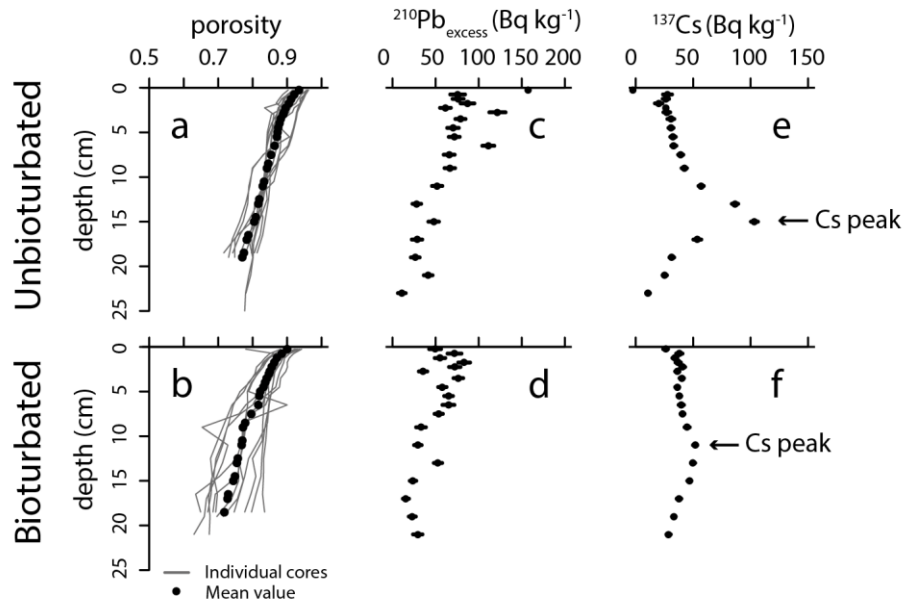
355

356 3.2 Porosity, radionuclides (²¹⁰Pb, ¹³⁷Cs) and sediment accumulation rate

357 All porosity profiles started from a similar high value (~0.95) and decreased with depth (Fig.
 358 2a,b), consistent with the effect of compaction on marine sediments (Boudreau et al., 1998).
 359 The porosity-depth profile did not differ between sampling campaigns, but porosity profiles in
 360 the bioturbated cores showed more variability than in unbioturbated cores (Fig. 2a,b), consistent
 361 with an increase in textural heterogeneity due to burrowing fauna. Solid-phase density did not
 362 show any trend with depth (data not shown), nor was there any difference between pond types
 363 (Table 2). The unbioturbated ponds had a solid-phase density of 1.9 \pm 0.4 g cm⁻³, a median
 364 grain size of 13-21 μm and >74% of the particles were finer than 63 μm. The bioturbated ponds

365 had a solid-phase density of $2.0 \pm 0.5 \text{ g cm}^{-3}$, a median grain size of 11-16 μm and >85% of the
366 particles were finer than 63 μm . These solid-phase densities are lower than those of common
367 siliclastic sediments ($\sim 2.6 \text{ g cm}^{-3}$), which is likely due to the high organic matter content (> 5%
368 OC, see below) of the sediment.

369 The down-core variation in the $^{210}\text{Pb}_{\text{excess}}$ profiles is indicative for a variable depositional
370 environment (Fig. 2c,d). When applied to the $^{210}\text{Pb}_{\text{excess}}$ data from the unbioturbated pond, the
371 PF model (section 2.6) estimated a sedimentation flux of $J_s = 0.8 \pm 0.2 \text{ kg m}^{-2} \text{ yr}^{-1}$ and a
372 sedimentation velocity $v_{\text{sed}} = 0.3 \pm 0.1 \text{ cm yr}^{-1}$, which lies centrally within the wide range of
373 values previously estimated for the Blakeney salt marsh (0.05 – 0.7 cm yr^{-1} ; French, 1993). The
374 narrowly defined peak in the ^{137}Cs activity profile from the unbioturbated pond suggests that
375 the sediment has experienced very little mixing over the last decades. This contrasts with the
376 smoothed ^{137}Cs peak in the depth profile from the bioturbated pond, which is typical for well-
377 mixed sediments (Robbins et al., 1979) (Fig. 2e,f). The ^{137}Cs maxima can be found at 15 cm
378 depth in the unbioturbated pond, and at 11 cm depth in the bioturbated pond (Fig. 2e,f). If we
379 calculate a sedimentation flux according to eq. [2], we get at a ^{137}Cs -based sedimentation flux
380 $J_s = 0.91 \pm 0.08 \text{ kg m}^{-2} \text{ yr}^{-1}$ for the unbioturbated pond and $J_s = 0.86 \pm 0.08 \text{ kg m}^{-2} \text{ yr}^{-1}$ for the
381 bioturbated pond. Both values are indistinguishable from the sedimentation flux estimated
382 based on the ^{210}Pb profile in the unbioturbated pond ($0.8 \pm 0.2 \text{ kg m}^{-2} \text{ yr}^{-1}$; Table A2, Appendix
383 3). In the rest of this manuscript, we will use an average of all three estimates; $J_s = 0.9 \text{ kg m}^{-2}$
384 yr^{-1} and $v_{\text{sed}} = 0.3 \text{ cm yr}^{-1}$. This sedimentation flux is at the low end of the typical range for
385 shallow environments (range: 0.3 – 10 $\text{kg m}^{-2} \text{ yr}^{-1}$; Aller, 2014).



386

387

388

389

Figure 2: (a,b) Porosity depth profiles collected during 2015, 2016 and 2018 campaigns. (c,d) Excess ^{210}Pb depth profiles and (e,f) ^{137}Cs depth profiles collected in 2015. The Cs peak is indicated by the arrow and corresponds to the year 1963. Data are given for unbioturbated (top row) and bioturbated (bottom row) ponds

390

391 3.3 Solid-phase chemistry

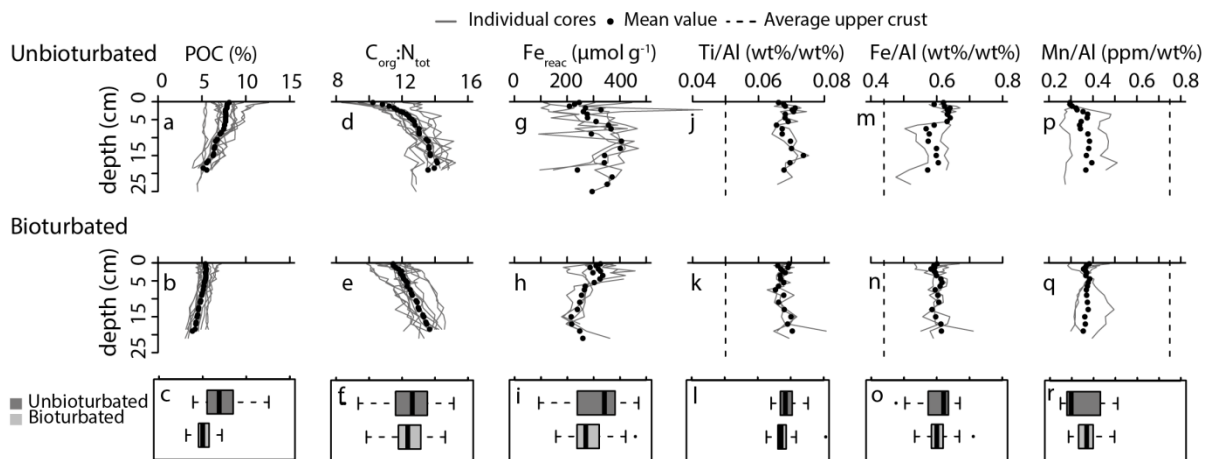
392 Particulate organic carbon (POC) contents and $C_{\text{org}}:N_{\text{tot}}$ ratios were measured on duplicate
 393 cores from each pond type in 2015 and 2016, as well as in duplicate cores from 4 different
 394 ponds of each pond type in 2018. POC depth profiles showed considerable variation, suggesting
 395 spatial heterogeneity in local input, possibly due to differences in macroalgal coverage (Fig.
 396 3a,b). Overall, the depth-averaged POC was significantly higher in the unbioturbated ponds (7
 397 ± 2 %) than in the bioturbated ponds (5.1 ± 0.9 %) (One-way ANOVA, $F\text{-value}_{1,10} = 15.53$, $p =$
 398 0.003) (Fig. 3c).

399 The depth averaged $C_{\text{org}}:N_{\text{tot}}$ ratios (11-13; Table 2, Fig. 3d,e,f) were not significantly
 400 different between pond types (One-way ANOVA, $F\text{-value}_{1,10} = 0.195$, $p = 0.67$), and are
 401 substantially lower than the C:N ratio of the common salt marsh vegetation (18-74) at the field
 402 site (Table 2). This suggests that ponds had the same source of organic matter, likely derived
 403 from a combination of marine (macroalgae, microphytobenthos) and terrestrial (surrounding
 404 marsh plants) origin. All cores showed an increase of the $C_{\text{org}}:N_{\text{tot}}$ ratio with depth, suggesting
 405 preferential nitrogen mineralisation. The gradient in the $C_{\text{org}}:N_{\text{tot}}$ ratio was less pronounced for
 406 the bioturbated cores, as expected from sediment bio-mixing (Fig. 3d,e).

407 Reactive iron was measured on duplicate cores from each pond type in 2015 and 2016. Total
 408 reactive iron ($\text{Fe}_{\text{reac}} = \text{Fe}_{\text{AVS}} + \text{Fe}_{\text{carb}} + \text{Fe}_{\text{ox1}} + \text{Fe}_{\text{ox2}} + \text{Fe}_{\text{mag}} + \text{Fe}_{\text{pyr}}$) showed substantial variation
 409 between depth profiles (Fig. 3g,h), but all cores had a similar depth-averaged iron content (280-

410 300 $\mu\text{mol g}^{-1}$) (Fig. 3i) (no statistics were done because of the small number of replicates; n =
 411 2 for each treatment).

412 Total solid-phase contents of Al, Ti, Fe and Mn were determined on sediment cores collected
 413 in 2015 and 2016. Depth profiles of Ti/Al, Fe/Al and Mn/Al are indistinguishable between
 414 ponds, indicating that sites receive similar detrital inputs (Fig. 3j-r). All profiles deviate from
 415 the ratio of the average upper crust, which is not unexpected since they represent an isolated
 416 system, which can receive detrital matter of a given signature that does not need to represent
 417 the averaged signal of the upper crust.



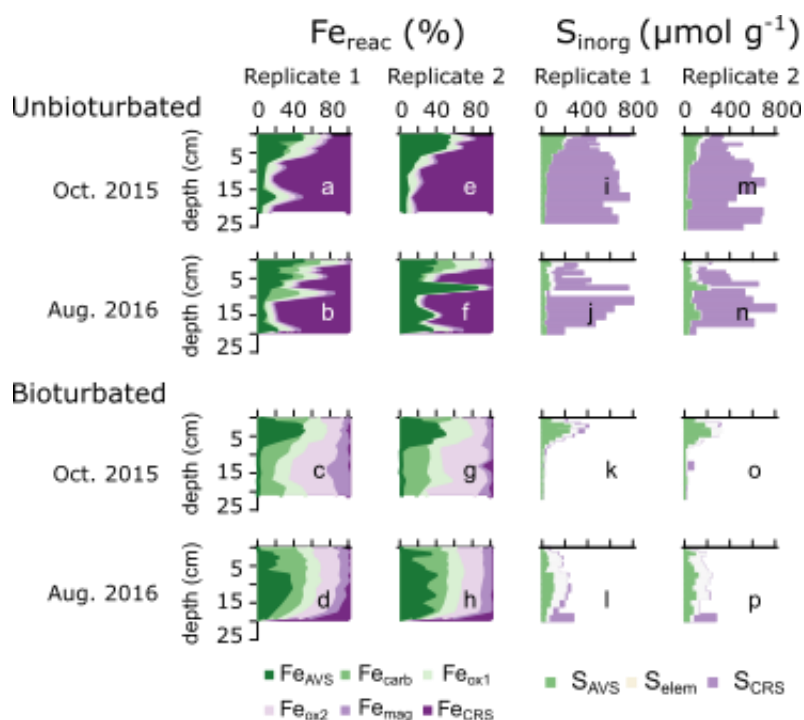
418
 419 **Figure 3:** Vertical depth profiles of (a)-(b) particulate organic carbon (POC) collected in 2015, 2016 and 2018, (d)-(e) C:N
 420 ratio of organic matter ($C_{\text{org}}:N_{\text{tot}}$) collected in 2015, 2016 and 2018, (g)-(h) total solid-phase reactive iron (Fe_{react}) collected in
 421 2015 and 2016, (j)-(q) solid-phase element ratios collected in 2015 and 2016 recorded in the unbioturbated (top row) and
 422 bioturbated ponds (bottom row). (c)-(i) boxplots of the concentrations per pond type. Concentrations are expressed in $\mu\text{mol g}^{-1}$
 423 of dry sediment for Fe_{react} or in mass % (gram per gram of dry sediment) for POC, ratios are in wt%/wt% ($C_{\text{org}}:N_{\text{tot}}$, Ti/Al and
 424 Fe/Al) or ppm/wt% (Mn/Ti). The dashed line is the ratio of the average upper crust, following McLennan (2001); Ti/Al = 0.05
 425 wt%/wt%, Fe/Al = 0.44 wt%/wt%, Mn/Al = 0.75 ppm/wt%.

426 3.4 Iron and sulphur speciation

427 Solid-phase iron and sulphur speciation was determined on duplicate cores for each pond
 428 type in 2015 and 2016. Duplicate cores showed good agreement (Fig. 4). The depth profiles of
 429 iron speciation showed strong similarity between seasons but marked differences between pond
 430 types. In the unbioturbated cores, the oxidised fractions (Fe_{ox1} , Fe_{ox2} , Fe_{mag}) contributed $\sim 30\%$
 431 to the total pool of reactive iron (Fe_{react}) in the upper 5 cm, after which their importance
 432 decreased to $<10\%$ in the deeper layers. Iron mono-sulphides (Fe_{AVS}) were the major
 433 component in the upper 5 cm ($\sim 50\%$), below 5 cm pyrite (Fe_{pyr}) became the dominant fraction
 434 ($> 80\%$ at 20 cm depth; Fig. 4a,b,e,f). In contrast, in the bioturbated pond, the oxidised fractions
 435 (Fe_{ox1} , Fe_{ox2} , Fe_{mag}) were dominant throughout the cores (50 – 100 %; Fig. 4c,d,g,h), while
 436 Fe_{AVS} build-up was restricted to the upper layers in 2015 ($\sim 50\%$ at 5 cm), after which it
 437 decreased to 0 % below 10 cm. In 2016, the oxidised fractions (Fe_{ox1} , Fe_{ox2} , Fe_{mag}) were also
 438 dominant, and the AVS build-up was limited and restricted to the deeper layers ($\sim 20 - 30\%$ of

439 the Fe_{react} pool). In the deepest sediment layer analysed (at 19 cm depth), pyrite suddenly became
440 important (~50 % of the Fe_{react} pool; Fig. 4d,h). This feature was present in both duplicate cores,
441 suggesting this is not an artefact.

442 Inorganic sulphur (S_{inorg}) rapidly accumulated with depth in the unbioturbated cores. In the
443 first 5 cm, AVS was the most important fraction (~200 $\mu\text{mol g}^{-1}$) in the total S_{inorg} pool, while
444 S^0 was only a small constituent. Below ~10 cm depth, pyrite became the major component (>
445 90 %) of the total S_{inorg} pool (Fig. 4i,m). In 2016, S^0 remained a minor constituent, while AVS
446 did not show an accumulation, and stayed constant (50 - 100 $\mu\text{mol g}^{-1}$) throughout the core (Fig.
447 4j,n). In the bioturbated cores of 2015, AVS showed an accumulation in the upper 10 cm (up
448 to 200 $\mu\text{mol g}^{-1}$), that disappeared with depth without being converted to S_{CRS} (Fig. 4k,o). In
449 2016, AVS accumulated slowly to ~150 $\mu\text{mol g}^{-1}$ at 10 cm depth, and subsequently decreased
450 with depth (Fig. 4l,p). The small amounts of pyrite found throughout the cores were likely an
451 artefact from the extraction procedures (pyrite is determined as the difference between the CRS
452 fraction and the S^0 extraction). Nevertheless, the increased pyrite concentration in the last
453 sediment section of 2016 was found in both replicates, which indicates that this is likely not an
454 artefact. Pyrite appeared below 20 cm depth, which correlates with the expected burrowing
455 depth of local burrowing species *Nereis diversicolor* (15-20 cm; Esselink and Zwarts, 1989)
456 and *Arenicola Marina* (15-25 cm; Rijken, 1979). Visual evidence of burrows and defaecation
457 mounds suggested the presence of both these species in the bioturbated ponds (Fig. A4,
458 Appendix 4).

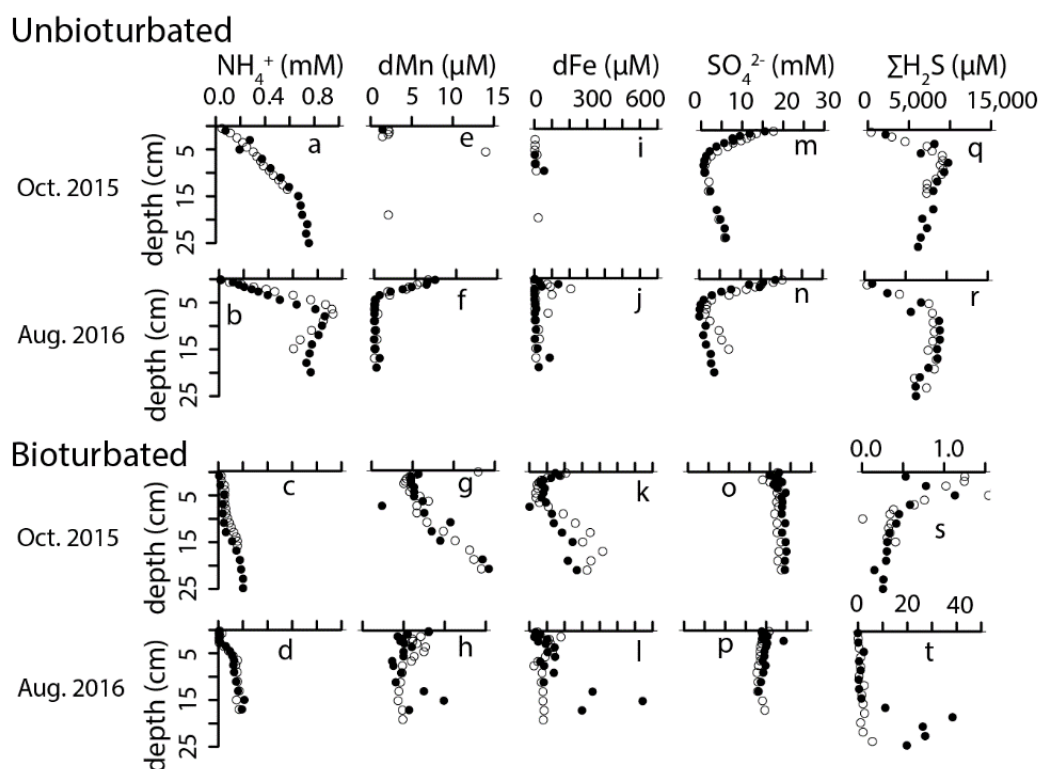


459
 460 **Figure 4:** Vertical depth profiles of (a)-(h) reactive iron speciation (Fe_{reac}), (i)-(p) inorganic sulphur speciation (S_{inorg}) recorded
 461 in the unbioturbated (upper two rows) and bioturbated ponds (lower two rows) in 2015 and 2016. The results in column one
 462 and three are from the same core, while the results in the second and fourth column are also from the same core.

463 3.5 Pore-water geochemistry

464 Overall, pore-water profiles for different solutes showed a good correspondence between
 465 duplicates and revealed a marked difference between bioturbated and unbioturbated sediments.

466 In 2015, ammonium (NH_4^+) accumulated with depth in the unbioturbated cores, gradually
 467 increasing to a value of 0.8 mM (Fig. 5a). In 2016, NH_4^+ accumulation occurred much faster
 468 and showed a subsurface maximum of 1 mM at 6 cm depth, below which NH_4^+ decreased to
 469 0.5-0.8 mM at 20 cm (Fig. 5b). This difference in concentration gradient was reflected in the
 470 diffusive fluxes near the SWI; the diffusive flux out of the sediment in 2015 was about 4 times
 471 lower than in 2016 (Table 3). In contrast, the bioturbated cores showed limited NH_4^+
 472 accumulation in the first ~2-5 cm, after which the concentrations remained at a low value ~0.2
 473 mM (Fig. 5c,d). This is most likely caused by burrow flushing, which promotes exchange of
 474 NH_4^+ with the overlying water, as well as nitrification and the precipitation of metal (Mn)
 475 oxides (which can oxidise NH_4^+), by input of oxygen, which limits its accumulation in the pore
 476 water.



477

478 **Figure 5:** Vertical depth profiles of pore-water solutes collected in 2015 and 2016. Profiles were recorded in the unbioturbated
 479 (upper two rows) and bioturbated ponds (lower two rows). (a)-(d) ammonium (NH_4^+), (e)-(h) dissolved manganese (dMn), (i)-
 480 (l) dissolved iron (dFe), (m)-(p) Sulphate normalised to chloride (see main text for details) (SO_4^{2-}) and (q)-(t) dissolved free
 481 sulphide ($\Sigma\text{H}_2\text{S}$). Note the difference in scale in the $\Sigma\text{H}_2\text{S}$ concentration in panels (q) and (r) versus (s) and (t). Filled and open
 482 symbols in the same panel indicate replicate cores.

483

484 The overall low concentrations of pore-water manganese (dMn) shows that manganese
 485 cycling was most likely not important at the field site. Dissolved Mn was undetectable in the
 486 unbioturbated cores of 2015 (Fig. 5e, the data point at 5 cm is likely a contamination), and was
 487 only present in very low concentrations in the bioturbated cores, where it showed a small
 488 decrease from 5 μM to 3 μM at 5 cm, after which dMn increased again to 10 μM (Fig. 5g). The
 489 metal samples in 2016 were analysed by HR-ICP-MS, which allowed measurement of dMn and
 490 dFe to low concentrations. In the unbioturbated cores, dMn rapidly decreased from 7.5 μM at
 491 the SWI to below detection at 4 cm depth (Fig. 5f). In the bioturbated cores, dMn accumulated
 492 in the upper 5 cm to $\sim 7.5 \mu\text{M}$ and decreased to 5 μM below (Fig. 5h).

493 Depth profiles of dissolved iron showed a good correlation with the dMn profiles; dFe was
 494 also undetectable in unbioturbated cores of 2015 (Fig. 5i), while profiles from the bioturbated
 495 ponds were similar to dMn, with an initial decrease from 200 μM to $\sim 50 \mu\text{M}$ in the upper 5 cm,
 496 and a subsequent increase to $\sim 300 \mu\text{M}$ (Fig. 5k). In the unbioturbated cores of 2016, dFe was
 497 near the LOQ throughout the core (Fig. 5j). In the bioturbated cores, there was a small
 498 enrichment of dFe in the upper 5-10 cm ($\sim 200 \mu\text{M}$), after which the concentrations dropped to

499 below the LOQ (Fig. 5l). One replicate showed a peak in dFe concentration at depth, which was
 500 also present in the dMn profile (Fig. 5h,l), possibly caused by natural variability.

501 Sulphate profiles (normalised to Cl⁻, see section 2.4) were similar between campaigns in the
 502 unbioturbated pond (Fig. 5m,n) and indicated strong sulphate consumption. Diffusive sulphate
 503 uptake was calculated on the non-normalised profiles and amounted to 14.6 mmol S m⁻² d⁻¹ in
 504 2015 and 23.7 mmol S m⁻² d⁻¹ in 2016 (Table 3). Sulphate reduction is strongly dependent on
 505 temperature (Isaksen and Jørgensen, 1996), and thus the higher temperature in summer (17°C
 506 vs 10°C in October; Table 2) could have led to higher sulphate reduction. The increase in
 507 sulphate concentration below 10 cm was most likely due to upward diffusion of sulphate from
 508 below the sampled depth (there is evidence for a deep hypersaline water source that supplies
 509 sulphate from below; Mills et al., 2016). In the bioturbated cores, sulphate profiles were straight
 510 (Fig. 5o,p), which suggests that there was no net sulphate consumption, although cryptic
 511 sulphur cycling was likely occurring (Mills et al., 2016).

512 Free sulphide profiles were inversely correlated with the sulphate profiles. Strong sulphate
 513 consumption in the unbioturbated cores coincided with high sulphide accumulation (up to 10
 514 mM at 10 cm depth) (Fig.5q,s). Dissolved sulphide fluxes (calculated from the linear gradient
 515 in the upper 5-10 cm) were comparable in the unbioturbated cores (19.6 and 17.5 mmol m⁻² d⁻¹;
 516 Table 3), and these were in the same range as the diffusive sulphate uptakes (Table 3). In the
 517 bioturbated cores, sulphide concentrations were three orders of magnitude lower (µM range;
 518 Fig. 5s,t). The bioturbated core of 2015 showed a little sulphide accumulation (~1.5 µM) in the
 519 upper 5 cm, which correlated with the accumulation of inorganic sulphur in the solid phase
 520 (Fig. 4k,o and Fig. 5r). In 2016, sulphide concentrations only increased below 15 cm (~30 µM
 521 at 20 cm depth) (Fig. 5t).

522 **Table 3:** Fluxes at the sediment-water interface (J_{SWI}) and burial fluxes (J_{burial}) of solid-phase species and diffusive fluxes
 523 of solutes at the sediment-water interface ($J_{diff,SWI}$) and at the end of the sediment cores ($J_{diff,deep}$). *Diffusive fluxes were
 524 estimated based on the average concentration gradient of duplicate cores the same time. Positive fluxes are directed downwards.
 525 n.d. = not determined.

Analyte	Symbol	Unit	Value			
			Unbioturbated		Bioturbated	
			Oct. 2015	Aug. 2016	Oct. 2015	Aug. 2016
J_{SWI}						
Organic Carbon	POC	mmol C m ⁻² d ⁻¹	27 ± 9	18 ± 6	n.d.	n.d.
J_{burial}						
Organic Carbon	POC	mmol C m ⁻² d ⁻¹	10 ± 3	12 ± 4	7 ± 2	9 ± 3
Total Nitrogen	TN	mmol N m ⁻² d ⁻¹	0.7 ± 0.3	0.8 ± 0.3	0.5 ± 0.2	0.8 ± 0.3
Pyrite	FeS ₂	µmol FeS ₂ m ⁻² d ⁻¹	700 ± 300	400 ± 300	10 ± 8	100 ± 100

Acid volatile sulphide	FeS	$\mu\text{mol Fe m}^{-2} \text{ d}^{-1}$	30 ± 10	80 ± 30	5 ± 5	80 ± 40
Elemental Sulphur	S ⁰	$\mu\text{mol S}^0 \text{ m}^{-2} \text{ d}^{-1}$	3 ± 2	9 ± 5	13 ± 8	140 ± 70
Carbonate iron	Fe _{carb}	$\mu\text{mol Fe m}^{-2} \text{ d}^{-1}$	10 ± 10	0	130 ± 70	50 ± 30
Easily reducible iron oxides	Fe _{ox1}	$\mu\text{mol Fe m}^{-2} \text{ d}^{-1}$	90 ± 90	40 ± 20	100 ± 100	60 ± 20
Moderately reducible iron oxides	Fe _{ox2}	$\mu\text{mol Fe m}^{-2} \text{ d}^{-1}$	40 ± 40	14 ± 6	300 ± 100	120 ± 40
Magnetite iron	Fe _{mag}	$\mu\text{mol Fe m}^{-2} \text{ d}^{-1}$	50 ± 40	27 ± 9	90 ± 50	70 ± 20
Total reactive iron	Fe _{reac}	$\mu\text{mol Fe m}^{-2} \text{ d}^{-1}$	900 ± 300	600 ± 300	600 ± 200	500 ± 100
<i>J_{diff,SWI} *</i>						
Ammonium	NH ₄ ⁺	$\text{mmol N m}^{-2} \text{ d}^{-1}$	-0.51	-2.01	-0.11	0
Dissolved iron	dFe	$\text{mmol Fe m}^{-2} \text{ d}^{-1}$	n.d.	-0.3	-0.15	-0.1
Sulphate	SO ₄ ²⁻	$\text{mmol S m}^{-2} \text{ d}^{-1}$	14.6	23.7	0	0
Dissolved sulphide	ΣH ₂ S	$\text{mmol S m}^{-2} \text{ d}^{-1}$	-19.6	-17.5	-0.001	0
<i>J_{diff,deep} *</i>						
Ammonium	NH ₄ ⁺	$\text{mmol N m}^{-2} \text{ d}^{-1}$	-0.03	0.1	-0.02	-0.03
Dissolved iron	dFe	$\text{mmol Fe m}^{-2} \text{ d}^{-1}$	n.d.	0	-0.03	0
Sulphate	SO ₄ ²⁻	$\text{mmol S m}^{-2} \text{ d}^{-1}$	-1.4	-1.4	0	0
Dissolved sulphide	ΣH ₂ S	$\text{mmol S m}^{-2} \text{ d}^{-1}$	1.2	0.6	0	0

526

527 4. DISCUSSION

528 4.1 External inputs and redox dichotomy

529 Our dataset confirms the redox dichotomy that has previously been observed in the pond
530 sediments of East Anglian salt marshes (Antler et al., 2019; Hutchings et al. (2019)). There is
531 iron-rich sediment, characterised by high ferrous iron pore-water concentrations (up to 0.6 mM
532 in the upper 30 cm; Fig. 5k,l) and sulphide-rich sediment, characterised by high pore-water
533 sulphide concentrations (up to 10 mM in the upper 30 cm; Fig. 5q,r). Even though both pond
534 types exhibit seasonal and spatial variability in their chemistry (Figs. 3-5), the differences
535 between iron-rich and sulphide-rich sediments are a clear feature of the East Anglian salt
536 marshes. To explain the origin of the redox dichotomy within these salt marshes (Fig. 1c),
537 Hutchings et al. (2019) carried out an aerial survey of two East Anglian marsh systems. They
538 proposed that a ponds proximity to a creek could potentially determine the pond subsurface
539 geochemistry, with iron-rich ponds tending to be closer to large creeks than sulphide-rich
540 ponds. The spatial positioning would then impose different boundary conditions, which could
541 alter the surface/subsurface delivery of iron and/or the surface delivery of organic carbon
542 (Spivak et al., 2017; Hutchings et al., 2019).

543 We can test these hypotheses with the current dataset. If a pond receives an increased
 544 delivery of dissolved reactive iron, this would also imply that the reactive iron inventory of the
 545 iron-rich pond would be systematically higher (as the supply is higher). However, neither the
 546 iron speciation (Fig. 3i), nor the estimated burial rates of reactive iron (Table 3), indicate any
 547 systematic difference in total reactive iron supply between the two pond types. If anything, the
 548 reactive iron burial rates suggest a higher iron supply in the sulphide-rich ponds (Table 3), in
 549 contrast to what would be expected (this could also be caused by some lateral diffusional loss
 550 from the iron-rich pond sediments to the surrounding soil; Antler et al., 2019). Additionally,
 551 solid-phase Fe/Al (Fig. 3o) were very similar between the two pond types, also suggesting that
 552 the two pond types are comparable in terms of reactive iron input.

553 Because of their specific positioning on the marsh, pond types could also potentially differ
 554 in the quality and/or quantity of the organic matter they receive. Foremost, a difference in
 555 quality is unlikely, as the C:N ratio of organic matter was comparable (~12) in all ponds
 556 investigated (Fig. 3f), which suggests that the organic matter source was similar, if not identical,
 557 in both pond types. Moreover, the C:N ratio of the salt marsh vegetation surrounding the ponds
 558 is considerably higher (18-74; Table 2), suggesting that the sedimentary organic matter was
 559 predominantly derived from local growth of marine algae in the ponds (macro-algae and/or
 560 microalgae) or from input of suspended marine POC. Pond sediments in temperate salt marsh
 561 systems on the US East Coast (MA, USA) have similar C:N ratios (~10), and stable isotope
 562 studies have shown most organic carbon is derived from local microalgae growth in the ponds
 563 (Spivak et al., 2017; Spivak et al., 2018).

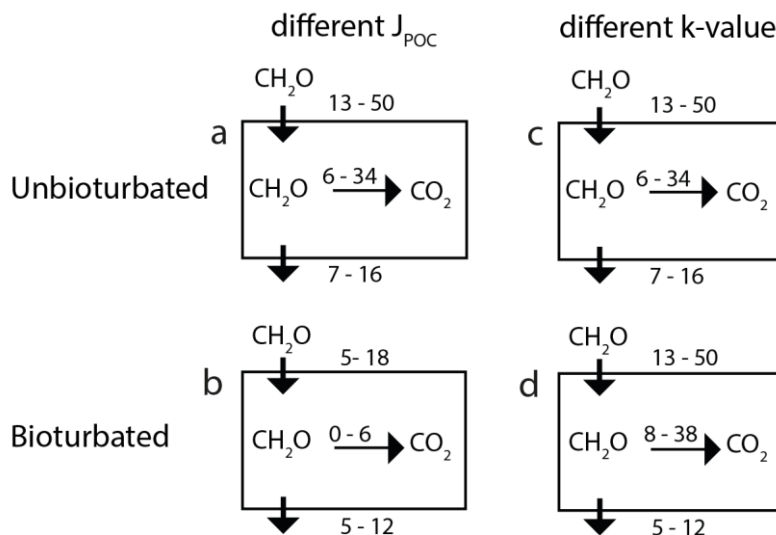
564 Our data indicate, however, that the quantity of organic matter (Fig. 3c) is significantly
 565 different between the two pond type sediments (mean POC 5.1 ± 0.9 % in bioturbated versus 7
 566 ± 2 % in unbioturbated). To analyse the cause of this difference, we establish a simple mass
 567 budget for organic carbon and obtain a relation for the key factors that control the magnitude
 568 of the mean POC (\hat{C}) (see Appendix 2 for the full derivation)

$$569 \quad \hat{C} = \frac{J_{input}}{(kL + v_{sed})} \quad [6]$$

570 where J_{input} is the input flux of organic carbon, v_{sed} is the sedimentation velocity, k is the first-
 571 order degradation constant, and L is the depth of the sediment interval. Our radionuclide data
 572 indicate that the sedimentation velocity v_{sed} is 0.3 cm yr^{-1} , and that it is similar in both the
 573 bioturbated and unbioturbated ponds (see section 3.2). So, if the mean POC is lower in the
 574 bioturbated ponds, Eq. [6] implies that either the organic input J_{input} is lower in the bioturbated

575 ponds, or that the intrinsic mineralisation rate k must be greater in the presence of burrowing
 576 fauna (or a combination of both).

577 We contend that a stimulation of organic matter mineralisation by fauna is a more likely
 578 explanation than a differential input of organic matter. If we assume that differential organic
 579 matter input alone is the cause of the concentration difference, then equation [6] predicts that
 580 the POC input into unbioturbated ponds should be ~37% higher than in bioturbated ponds
 581 (Appendix 2). The estimated organic matter input in the unbioturbated ponds is 13 - 50 mmol
 582 C m⁻² d⁻¹ (see Appendix 2 for the calculations). A 37% decrease is substantial and would lead
 583 to reduced mineralisation rates in the bioturbated ponds (Fig. 6a,b). Such a big difference in
 584 POC input would also be difficult to reconcile with the proximity of both types of ponds on the
 585 marsh. Instead, we advance that the differences observed within the ponds are mainly related
 586 to the presence of bioturbating fauna. If we assume that organic matter input in both ponds
 587 types is the same, and that the observed difference in POC concentrations solely results from
 588 the presence of the burrowing macrofauna, then bioturbation could stimulate the rate of organic
 589 matter mineralisation by 12-33 % (Fig. 6c,d; Appendix 2). Previous laboratory incubation
 590 studies have estimated increases in mineralisation rates due to bioturbation from 50 % to 275
 591 % (Kristensen et al., 1992; Banta et al., 1999; Bianchi et al., 2000; Heilskov and Holmer, 2001;
 592 Papaspyrou et al., 2007; Papaspyrou et al., 2010; Nascimento et al., 2012). These values are
 593 higher than our estimate and are likely an overestimation of the effects observed in the field
 594 (Welsh, 2003), suggesting that the observed decrease in POC could well be due to macrofauna.



595

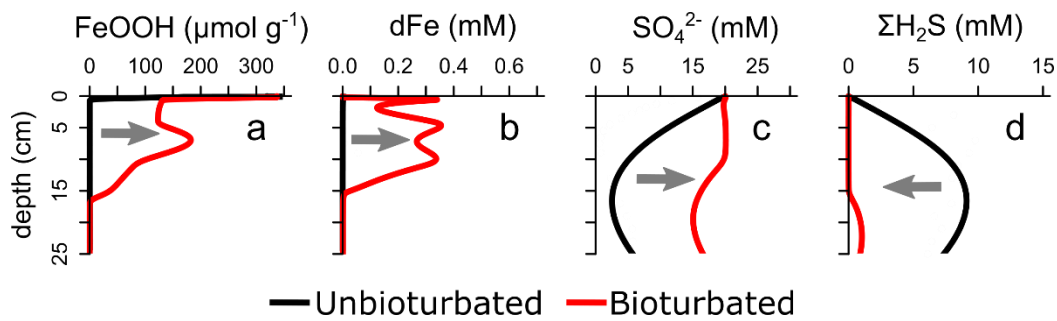
596 **Figure 6:** A rudimentary mass budget for organic carbon, following equation [6]. All fluxes in mmol C m⁻² d⁻¹. See main text
 597 and Appendix 2 for details.

598

599 4.2 Bioturbation stimulates iron and sulphur recycling

600 To better understand the redox dichotomy observed in the pond sediments, we have
601 constructed an early diagenetic ‘ideal world’ model based on our field observations (Appendix
602 1) to compare two sediment columns, one without and one with bioturbation (Figure 7). We
603 use these model results to qualitatively illustrate the effect of bioturbation on the depth profiles
604 of key iron (Fe^{2+} and FeOOH) and sulphur species (SO_4^{2-} and $\Sigma\text{H}_2\text{S}$). Additionally, we have
605 compiled quantitative estimates of Fe and S cycling numbers (the number of times an element
606 cycles between its oxidised and reduced state; Eq. [5]) in bioturbated and unbioturbated
607 sediments from the literature (Table 4). Note that these modelling results assume that the
608 sediment columns are in steady state, which is likely not the case for our salt marsh system.
609 Nevertheless, this modelling exercise does help to illustrate the impact of bioturbating fauna on
610 sedimentary Fe-S cycling.

611 In an unbioturbated sediment, the diagenetic model predicts that organic matter
612 mineralisation is driven by sulphate reduction (leading to SO_4^{2-} depletion; Fig. 7d), while
613 FeOOH is directly transformed to FeS and FeS_2 (Fig. 7a) and dissimilatory iron reduction is
614 suppressed. As a result, free sulphide builds up to high concentrations in the pore water (Fig.
615 7d), while ferrous iron (Fe^{2+}) remains low (Fig. 7b). These same features are seen in our field
616 pore-water data from the unbioturbated sediment (Fig. 5). Overall, an unbioturbated sediment
617 is characterized by low levels of Fe and S recycling. The trapping of Fe(II) as $\text{FeS}_{(2)}$ limits its
618 upward diffusion to the oxic zone, and thus inhibits its re-oxidation by oxygen, nitrate or
619 manganese oxides, which restricts the internal Fe recycling (Widerlund and Ingri, 1996).
620 Similarly, the absence of biomixing implies that FeS and FeS_2 are not transported back into the
621 oxic zone. This should limit the re-oxidation of reduced sulphide and hence reduce the S
622 recycling. While field studies suggest no Fe and S recycling in unbioturbated sediments ($N_S \sim$
623 $N_{\text{Fe}} \sim 1$; Table 4), model simulations do predict higher cycling numbers ($N_S \sim 5-6$; $N_{\text{Fe}} \sim 10$;
624 Table 4). According to the diagenetic model, some iron and sulphur recycling must occur within
625 a narrow zone around the oxic-anoxic transition in the sediment (Fig. A5, Appendix 4; van de
626 Velde and Meysman, 2016). As this recycling occurs within a very narrow zone (micrometres),
627 it is very difficult to capture this process with the current core slicing procedures and analytical
628 measurements. More fine-scaled measurement methods (e.g., high resolution voltammetric
629 micro-electrode measurements or diffusive gradient in thin film methods; Anschutz et al., 2000;
630 Gao et al., 2015) should investigate whether this cycling is a model artefact, or a genuine
631 process occurring in the sediment.



633

634 **Figure 7:** Model results of two identical sediments, one without bioturbation (black line) and one with bioturbation (red line).
 635 Model set-up is described in Appendix 1, model scenario shown here is ‘B + SP’ and an irrigation rate of 1.2 yr⁻¹. (a) iron oxide
 636 (FeOOH), (b) dissolved iron (dFe), (c) sulphate (SO₄²⁻), (d) free sulphide (HS⁻). Grey arrow indicates the effect of bioturbation;
 637 the sediment becomes higher in iron content due to the stimulation of iron cycling, which limits the build-up of free sulphide.

638

639 The inclusion of bioturbation in the model substantially alters the biogeochemical cycling
 640 within the sediment (Figure 7). The in-flushing of O₂ through bio-irrigation sustains high
 641 concentrations of iron oxides in the upper 10 cm (Fig. 7a), consistent with our field observations
 642 (Figure 4a-h), and allows the build-up of dissolved Fe(II) in the pore water (Fig. 5k,l, Fig. 7a).
 643 Overall, bioturbated sediments are characterized by elevated levels of Fe and S recycling (Table
 644 4; van de Velde and Meysman, 2016). Bio-mixing results in an upward transport of FeS to the
 645 oxic zone and its oxidative dissolution (Canfield et al., 1993; Thamdrup et al., 1994), while bio-
 646 irrigation creates an additional influx of O₂ at depth, which also triggers the oxidation of free
 647 sulphide and ferrous iron (Berner and Westrich, 1985; Aller and Aller, 1998). Both model
 648 studies and field assessments show that N_{Fe} and N_S values are substantially higher in bioturbated
 649 than in unbioturbated sediments (Table 4).

650 Overall, the inclusion of bioturbation in the diagenetic model generates a transition from a
 651 sulphur-dominated to an iron-dominated sediment (Fig. 7), which closely reproduces the
 652 dichotomy that is seen in our field data (Fig. 5). By stimulating Fe recycling, bioturbation limits
 653 the accumulation of free sulphide in the pore water (Figure 7d), and promotes the accumulation
 654 of ferrous iron. As a result, the sediment changes from a sulphur-dominated systems to an iron-
 655 dominated system (Figure 7), consistent with our field observations (Fig. 5).

656

Element		Cycling number	Reference
Fe - unbioturbated	Field data	1	(Widerlund and Ingri, 1996)
	Modelling	10	(van de Velde and Meysman, 2016)
Fe - bioturbated	Field data	4 - 21	(Thibault de Chanvalon et al., 2017)
	"	1 - 2.5	(Slomp et al., 1997)

	"	15	(Thamdrup et al., 1994)
	"	130 - 300	(Canfield et al., 1993)
	"	8	(Krom et al., 2002)
	"	4 - 453	(Esch et al., 2013)
	Modelling	40	(van de Velde and Meysman, 2016)
	"	9	(Wijsman et al., 2001)
	"	9 - 13	(Van Cappellen and Wang, 1996)
S - unbioturbated	<i>Field data</i>	1 - 3	(Middelburg, 1991)
	"	1 - 4	(Berner and Westrich, 1985)
	"	1	(Chanton et al., 1987)
	Global estimate	1 - 5	(Canfield and Farquhar, 2009)
	Modelling	5 - 6	(van de Velde and Meysman, 2016)
S - bioturbated	<i>Field data</i>	10	(Jørgensen, 1977)
	"	7 - 17	(Berner and Westrich, 1985)
	"	17	(Chanton et al., 1987)
	"	59	(Fallon, 1987)
	"	17	(Swider and Mackin, 1989)
	Global estimate	33	(Canfield and Farquhar, 2009)
	Modelling	10	(van de Velde and Meysman, 2016)

657 **Table 4:** Literature estimations of cycling numbers for Fe and S. See Eq. [5] for how cycling numbers have been calculated.

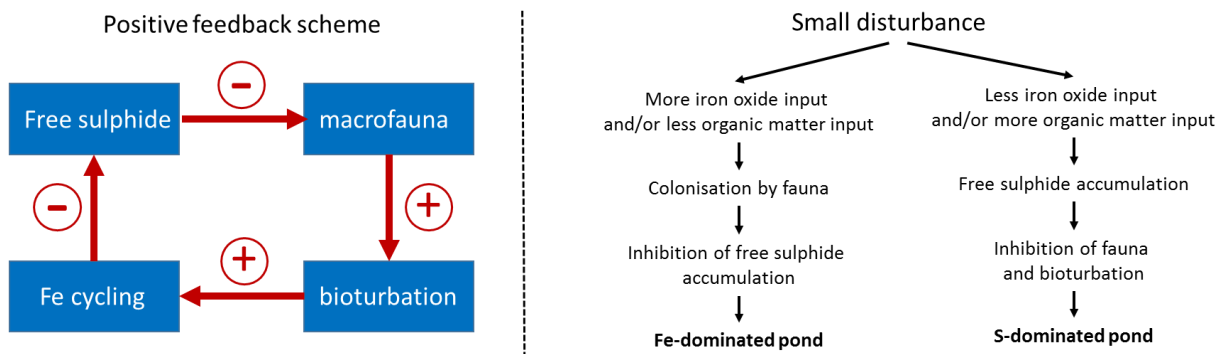
658 **4.3 Alternative stable states in iron-sulphur cycling**

659 We have shown that the differences in input fluxes between pond types are likely small
660 (section 4.1), so that these cannot act as the direct drivers of the observed redox dichotomy
661 (large differences in redox chemistry would require large variations in solid-phase carbon and
662 iron inputs). Instead, our results suggest that the presence/absence of bioturbation is the driving
663 force behind the observed dichotomy in redox chemistry (section 4.2). Note, however, that this
664 does not fully resolve the “redox dichotomy” conundrum. It simply replaces the old question
665 (how can ponds only meters apart have a completely different redox chemistry?) with a new
666 one (how can ponds only meters apart have completely different bioturbation conditions?).

667 We propose that the key lies in the close interplay between the early diagenetic cycles of
668 iron and sulphur, small differences in solid-phase inputs and the superimposed effect of
669 bioturbation on the coupled Fe-S cycles. We advance that non-linear interactions in the Fe-S
670 cycles can generate alternative stable states, in which small differences in inputs can be
671 amplified by positive feedbacks. The general scheme of how such alternative stable states can
672 be generated is depicted in Figure 8. The positive feedback loop starts with the fact that free
673 sulphide is generally toxic to animals and the accumulation of free sulphide in the pore water
674 would inhibit the colonisation of the sediment by fauna. Less fauna implies less bioturbation.
675 Hence, as discussed above, this increases the importance of sulphate reduction relative to
676 dissimilatory iron reduction, leading to high amounts of free sulphide in the pore water (Figure
677 7a), which then excludes bioturbation, limits the internal recycling of Fe and reinforces the

678 accumulation of free sulphide. Altogether this provides a positive feedback (Figure 8a), and the
 679 presence of such feedbacks has been demonstrated to generate alternative stable states in a range
 680 of natural systems, including the P cycling in shallow lakes and diatom growth in coastal
 681 systems (Van de Koppel et al., 2001; Carpenter, 2005).

682 By means of a positive feedback, a small initial perturbation in the sedimentary redox state
 683 of the ponds can be amplified, promoting a chemistry flip either to an S-dominated or an Fe-
 684 dominated state (Figure 8b). For example, one can imagine a scenario in which a small
 685 disturbance occurs and less organic matter arrives at the sediment (e.g. the pond is flushed just
 686 before winter and the algae biomass in the overlying water is removed). Following that
 687 disturbance, less sulphide will be produced in the pore water. This may allow some burrowing
 688 faunal species to colonise the sediment, which then stimulates the redox recycling of Fe within
 689 the sediment, thus reducing free sulphide concentrations and improving the living conditions
 690 for other macrofauna. The pond would then rapidly evolve to a Fe-dominated redox state.
 691 Alternatively, if the pond initially received an elevated input of organic matter, sulphide would
 692 accumulate in the pore water, preventing the colonisation of burrowing fauna. This would
 693 reduce the redox recycling of Fe within the sediment, stimulating the accumulation of free
 694 sulphide to higher levels, which keep out bioturbators. In this way, for near-identical boundary
 695 conditions, one can thus have two contrasting redox conditions.



696

697 **Figure 8:** (a) Proposed mechanism for a positive feedback in Fe/S cycling in salt marsh ponds (b) Proposed sequence of events
 698 leading to the observed sedimentary redox dichotomy in salt marsh ponds.

699

700 5. SUMMARY, CONCLUSIONS AND OUTLOOK

701 Bioturbation has a major impact on the redox cycling of carbon, iron and sulphur in aquatic
 702 sediments. We compared two identical sedimentary settings, where the main difference was the
 703 presence of bioturbation. Based on *in-situ* observations, we have shown that bioturbation
 704 stimulates organic matter mineralisation by 12-33 %. The presence of burrowing of marine

705 fauna also stimulated iron cycling at the expense of sulphur cycling. Overall, our results
706 illustrated how the presence of burrowing fauna drives the sedimentary redox chemistry from
707 a sulphide-dominated state to an iron-dominated state.

708 The salt marsh complexes along the East Anglian (UK) coast are characterised by an
709 intriguing redox dichotomy. Pond sediments can be classified either as sulphide-dominated and
710 unbioturbated or iron-dominated and bioturbated. We have shown that the presence or absence
711 of bioturbators are the likely driving force behind the observed redox dichotomy in the salt
712 marsh complexes. We propose that the seemingly random distribution of bioturbated and
713 unbioturbated ponds is caused by small differences in solid-phase inputs and the non-linear
714 interactions in the coupled Fe-S cycles, which can generate alternative stable states, in which
715 small differences in inputs can be amplified by positive feedbacks. To test this hypothesis
716 further, an in-depth model analysis of the coupled cycles of carbon, iron and sulphur in marine
717 sediments is required. Moreover, the strong non-linear interaction between iron and sulphur
718 cycling is not a specific feature of salt marsh sediments, but applies to many more types of
719 marine sediments, and hence suggests that alternative stable states in redox cycling could also
720 be present in other marine systems.

721 **6. ACKNOWLEDGEMENTS**

722 The research leading to these results was financially supported by the Belgian American
723 Educational Foundation (postdoctoral fellowship to SVDV) and the Research Foundation
724 Flanders (PhD fellowship to SVDV). FJRM was financially supported by the European
725 Research Council under the European Union's Seventh Framework Program (FP/2007-2013)
726 through ERC Grant 306933, by the Research Foundation Flanders via FWO grant G031416N,
727 and the Netherlands Organization for Scientific Research (VICI grant 016.VICI.170.072). The
728 HR-ICP-MS instrument was financed by the HERCULES Foundation (Code: UABR/11/010).
729 The authors would like to thank Jurian Brassler, Peter Van Breugel, Jan Sinke, Jan Peene,
730 Yvonne van der Maas, Pieter Van Rijswijk of NIOZ Yerseke and David Verstraeten of the Vrije
731 Universiteit Brussel for the analysis of the pore-water and sediment samples. Additionally, we
732 would like to thank Kirsten Imhoff and Timothy F. Ferdelman from the Max Planck Institute
733 for Marine Microbiology for the analysis of the elemental sulphur samples.

734 **7. References**

- 735 Aller R. C. (2014) Sedimentary Diagenesis, Depositional Environments, and Benthic Fluxes.
736 In *Treatise on Geochemistry* (2nd ed.) Elsevier Ltd. pp. 293–334. Available at:
737 <http://dx.doi.org/10.1016/B978-0-08-095975-7.00611-2>.
738 Aller R. C. (1977) The influence of macrobenthos on chemical diagenesis of marine
739 sediments. Yale University.

- 740 Aller R. C. and Aller J. Y. (1998) The effect of biogenic irrigation intensity and solute
741 exchange on diagenetic reaction rates in marine sediments. *J. Mar. Res.* **56**, 905–936.
- 742 Aminot A., K erouel R. and Coverly S. C. (2009) Nutrients in seawater using segmented flow
743 analysis. In *Practical guidelines for the analysis of seawater* (ed. O. Wurl). CRC press.
- 744 Anschutz P., Sundby B., Lefran ois L., Luther G. W. and Mucci A. (2000) Interactions
745 between metal oxides and species of nitrogen and iodine in bioturbated marine
746 sediments. *Geochim. Cosmochim. Acta* **64**, 2751–2763.
- 747 Antler G., Mills J. V., Huthings A., Redeker K. and Turchyn A. V. (2019) The sedimentary
748 carbon-sulfur-iron interplay - a lesson from East Anglian salt marsh sediments. *Front.*
749 *Earth Sci.* **7**, 140.
- 750 Appleby P. G. and Oldfield F. (1978) The calculation of lead-210 dates assuming a constant
751 rate of supply of unsupported 210Pb to the sediment. *Catena* **5**, 1–8.
- 752 Archer D. and Devol A. H. (1992) Benthic oxygen fluxes on the Washington shelf and slope:
753 A comparison of in situ microelectrode and chamber flux measurements. *Limnol.*
754 *Oceanogr.* **37**, 614–629.
- 755 Banta G. T., Holmer M., Jensen M. H. and Kristensen E. (1999) Effects of two polychaete
756 worms, *Nereis diversicolor* and *Arenicola marina*, on aerobic and anaerobic
757 decomposition in a sandy marine sediment. *Aquat. Microb. Ecol.* **19**, 189–204.
- 758 Berner R. A. and Westrich J. T. (1985) Bioturbation and the early diagenesis of carbon and
759 sulfur. *Am. J. Sci.* **285**, 193–206.
- 760 Bianchi T. S., Johansson B. and Elmgren R. (2000) Breakdown of phytoplankton pigments in
761 Baltic sediments: Effects of anoxia and loss of deposit-feeding macrofauna. *J. Exp. Mar.*
762 *Bio. Ecol.* **251**, 161–183.
- 763 Boudreau B. P. (1997) *Diagenetic Models and their Implementation.*, Springer-Verlag Berlin
764 Heidelberg New York.
- 765 Boudreau B. P. (1996) The diffusive tortuosity of fine-grained unlithified sediments.
766 *Geochim. Cosmochim. Acta* **60**, 3139–3142.
- 767 Boudreau B. P., Mucci A., Sundby B., Luther III G. W. and Silverberg N. (1998)
768 Comparative diagenesis at three sites on the Canadian continental margin. *J. Mar. Res.*
769 **56**, 1259–1284.
- 770 Canfield D. E. and Farquhar J. (2009) Animal evolution, bioturbation, and the sulfate
771 concentration of the oceans. *Proc. Natl. Acad. Sci.* **106**, 8123–8127.
- 772 Canfield D. E., Raiswell R., Westrich J. T., Reaves C. M. and Berner R. a. (1986) The use of
773 chromium reduction in the analysis of reduced inorganic sulfur in sediments and shales.
774 *Chem. Geol.* **54**, 149–155.
- 775 Canfield D. E., Thamdrup B. and Hansen J. W. (1993) The anaerobic degradation of organic
776 matter in Danish coastal sediments: iron reduction, manganese reduction, and sulfate
777 reduction. *Geochim. Cosmochim. Acta* **57**, 3867–3883.
- 778 Van Cappellen P. and Wang Y. (1996) Cycling of iron and manganese in surface sediments: a
779 general theory for the coupled transport and reaction of carbon, oxygen, nitrogen, sulfur,
780 iron, and manganese. *Am. J. Sci.* **296**, 197–243.
- 781 Carpenter S. R. (2005) Eutrophication of aquatic ecosystems: Bistability and soil phosphorus.
782 *Proc. Natl. Acad. Sci.* **102**, 10002–10005.
- 783 Chanton J. P., Martens C. S. and Goldhaber M. B. (1987) Biogeochemical cycling in an
784 organic-rich coastal marine basin. 7. Sulfur mass balance, oxygen uptake and sulfide
785 retention. *Geochim. Cosmochim. Acta* **51**, 1187–1199.
- 786 Cline J. D. (1969) Spectrophotometric Determination of Hydrogen Sulfide in Natural Waters.
787 *Limnol. Oceanogr.* **14**, 454–458.
- 788 Cornwell J. C. and Morse J. W. (1987) The characterization of iron sulfide minerals in anoxic
789 sediments. *Mar. Chem.* **22**, 193–206.

- 790 Crompton T. R. (1989) Metals. In *Analysis of Seawater* Butterworths & Co. pp. 74–215.
- 791 Dickson A. G., Afghan J. D. and Anderson G. C. (2003) Reference materials for oceanic CO₂
- 792 analysis: a method for the certification of total alkalinity. *Mar. Chem.* **80**, 185–197.
- 793 Available at: <http://www.sciencedirect.com/science/article/pii/S0304420302001330>.
- 794 Elrod V. A., Berelson W. M., Coale K. H. and Johnson K. S. (2004) The flux of iron from
- 795 continental shelf sediments: A missing source for global budgets. *Geophys. Res. Lett.* **31**,
- 796 2–5.
- 797 Esch M. E. S., Shull D. H., Devol A. H. and Moran S. B. (2013) Regional patterns of
- 798 bioturbation and iron and manganese reduction in the sediments of the southeastern
- 799 Bering Sea. *Deep. Res. Part II Top. Stud. Oceanogr.* **94**, 80–94. Available at:
- 800 <http://dx.doi.org/10.1016/j.dsr2.2013.04.004>.
- 801 Esselink P. and Zwarts L. (1989) Seasonal trend in burrow depth and tidal variation in feeding
- 802 activity of *Nereis diversicolor*. *Mar. Ecol. Prog. Ser.* **56**, 243–254.
- 803 Fallon R. D. (1987) Sedimentary sulfides in the Nearshore Georgia Bight. *Estuar. Coast.*
- 804 *Shelf Sci.* **25**, 607–619.
- 805 French J. R. (1993) Numerical simulation of vertical marsh growth and adjustment to
- 806 accelerated sea-level rise, North Norfolk, U.K. *Earth Surf. Process. Landforms* **18**, 63–
- 807 81.
- 808 Funnell B. and Pearson I. (1989) Holocene sedimentation on the North Norfolk barrier coast
- 809 in relation to relative sea-level change. *J. Quat. Sci.* **4**, 25–36.
- 810 Gao Y., van de Velde S., Williams P. N., Baeyens W. and Zhang H. (2015) Two-dimensional
- 811 images of dissolved sulfide and metals in anoxic sediments by a novel diffusive
- 812 gradients in thin film probe and optical scanning techniques. *TrAC - Trends Anal. Chem.*
- 813 **66**.
- 814 Gros N., Camões M. F., Oliveira C. and Silva M. C. R. (2008) Ionic composition of seawaters
- 815 and derived saline solutions determined by ion chromatography and its relation to other
- 816 water quality parameters. *J. Chromatogr. A* **1210**, 92–8. Available at:
- 817 <http://www.ncbi.nlm.nih.gov/pubmed/18829032> [Accessed December 3, 2014].
- 818 Heilskov A. C. and Holmer M. (2001) Effects of benthic fauna on organic matter
- 819 mineralization in fish-farm sediments: importance of size and abundance. *ICES J. Mar.*
- 820 *Sci.* **58**, 427–434.
- 821 Hutchings A. M., Antler G., Wilkening J., Basu A., Bradbury H. J., Clegg J. A., Gorka M.,
- 822 Lin C. Y., Mills J. V., Pellerin A., Redeker K., Sun X. and Turchyn A. V. (2019) Creek
- 823 dynamics determine pond subsurface geochemical heterogeneity in East Anglian (UK)
- 824 salt marshes. *Front. Earth Sci.* **7**, 41. Available at:
- 825 <https://www.frontiersin.org/articles/10.3389/feart.2019.00041/abstract> [Accessed March
- 826 6, 2019].
- 827 Isaksen I. and Jørgensen B. O. B. (1996) Adaptation of psychrophilic and psychrotrophic
- 828 sulfate-reducing bacteria to permanently cold marine environments. *Appl. Environ.*
- 829 *Microbiol.* **62**, 408–414.
- 830 Jones C. G., Lawton J. H. and Shachak M. (1994) Organisms as Ecosystem Engineers. *Oikos*
- 831 **69**, 373–386.
- 832 Jørgensen B. B. (1977) The sulfur cycle of a coastal marine sediment (Limfjorden). *Limnol.*
- 833 *Oceanogr.* **22**, 814–832.
- 834 Kallmeyer J., Ferdeman T. G., Weber A., Fossing H. and Jørgensen B. B. (2004) Evaluation
- 835 of a cold chromium distillation procedure for recovering very small amounts of
- 836 radiolabeled sulfide related to sulfate reduction measurements. *Limnol. Oceanogr.*
- 837 *Methods* **2**, 171–180.
- 838 Kamyshny A., Borkenstein C. G. and Ferdeman T. G. (2009) Protocol for Quantitative
- 839 Detection of Elemental Sulfur and Polysulfide Zero-Valent Sulfur Distribution in Natural

- 840 Aquatic Samples. *Geostand. Geoanalytical Res.* **33**, 415–435. Available at:
841 <http://doi.wiley.com/10.1111/j.1751-908X.2009.00907.x> [Accessed May 28, 2019].
- 842 Van de Koppel J., Herman P. M., Thoolen P. and Heip C. H. (2001) Do alternate stable states
843 occur in natural ecosystems? Evidence from a tidal flat. *Ecology* **82**, 3449–3461.
844 Available at: <https://www.jstor.org/stable/pdf/2680164.pdf> [Accessed May 15, 2019].
- 845 Kostka J. E., Gribsholt B., Petrie E., Dalton D., Skelton H. and Kristensen E. (2002) The rates
846 and pathways of carbon oxidation in bioturbated saltmarsh sediments. *Limnol.*
847 *Oceanogr.* **47**, 230–240.
- 848 Kostka J. E. and Luther III G. W. (1994) Partitioning and speciation of solid phase iron in
849 saltmarsh sediments. *Geochim. Cosmochim. Acta* **58**, 1701–1710.
- 850 Kristensen E., Andersen F. and Blackburn T. H. (1992) Effects of benthic macrofauna and
851 temperature on degradation macroalgal detritus: The fate of organic carbon. *Limnol.*
852 *Oceanogr.* **37**, 1404–1419.
- 853 Kristensen E., Penha-Lopes G., Delefosse M., Valdemarsen T., Quintana C. O. and Banta G.
854 T. (2012) What is bioturbation? the need for a precise definition for fauna in aquatic
855 sciences. *Mar. Ecol. Prog. Ser.* **446**, 285–302.
- 856 Krom M. D., Mortimer R. J. G., Poulton S. W., Hayes P., Davies I. M., Davison W. and
857 Zhang H. (2002) In-situ determination of dissolved iron production in recent marine
858 sediments. *Aquat. Sci.* **64**, 282–291. Available at:
859 <http://www.scopus.com/inward/record.url?eid=2-s2.0-0036438897&partnerID=tZOtx3y1>.
- 860
- 861 Lecroart P., Maire O., Schmidt S., Grémare A., Anschutz P. and Meysman F. J. R. (2010)
862 Bioturbation, short-lived radioisotopes, and the tracer-dependence of biodiffusion
863 coefficients. *Geochim. Cosmochim. Acta* **74**, 6049–6063.
- 864 McCave I. N. (1986) Evaluation of a laser-diffraction-size analyzer for use with natural
865 sediments. *J. Sediment. Res.* **54**, 561–564.
- 866 McLennan S. M. (2001) Relationships between the trace element composition of sedimentary
867 rocks and upper continental crust. *Geochemistry, Geophys. Geosystems* **2**.
- 868 Meysman F. J. R., Boudreau B. P. and Middelburg J. J. (2005) Modeling reactive transport in
869 sediments subject to bioturbation and compaction. *Geochim. Cosmochim. Acta* **69**, 3601–
870 3617. Available at: <http://linkinghub.elsevier.com/retrieve/pii/S0016703705000499>
871 [Accessed January 27, 2014].
- 872 Meysman F. J. R., Middelburg J. J. and Heip C. H. R. (2006) Bioturbation: a fresh look at
873 Darwin’s last idea. *Trends Ecol. Evol.* **21**, 688–95. Available at:
874 <http://www.ncbi.nlm.nih.gov/pubmed/16901581> [Accessed January 20, 2014].
- 875 Middelburg J. J. (1991) Organic carbon, sulphur, and iron in recent semi-euxinic sediments of
876 Kau Bay, Indonesia. *Geochim. Cosmochim. Acta* **55**, 815–828.
- 877 Mills J. V., Antler G. and Turchyn A. V. (2016) Geochemical evidence for cryptic sulfur
878 cycling in salt marsh sediments. *Earth Planet. Sci. Lett.* **453**, 23–32.
- 879 Nascimento F. J. a., Naslund J. and Elmgren R. (2012) Meiofauna enhances organic matter
880 mineralization in soft sediment ecosystems. *Limnol. Oceanogr.* **57**, 338–346. Available
881 at:
882 http://apps.webofknowledge.com/full_record.do?product=UA&search_mode=GeneralSearch&qid=6&SID=Y1AFLh5bIFOEdknDAF2&page=1&doc=1.
- 883
- 884 Nieuwenhuize J., Maas Y. E. M. and Middelburg J. J. (1994) Rapid analysis of organic
885 carbon and nitrogen in particulate materials. *Mar. Chem.* **45**, 217–224.
- 886 Pappaspyrou S., Kristensen E. and Christensen B. (2007) *Arenicola marina* (Polychaeta) and
887 organic matter mineralisation in sandy marine sediments: in situ and microcosm
888 comparison. *Estuar. Coast. Shelf Sci.* **72**, 213–222.
- 889 Pappaspyrou S., Thessalou-Legaki M. and Kristensen E. (2010) The influence of infaunal

890 (Nereis diversicolor) abundance on degradation of organic matter in sandy sediments. *J.*
891 *Exp. Mar. Bio. Ecol.* **393**, 148–157.

892 Pethick J. (1980) the Holocene transgression : initiation during the example of the North
893 Norfolk marshes, England. *J. Biogeogr.* **7**, 1–9.

894 Pethick J. S. (1974) The distribution of salt pans on tidal salt marshes. *J. Biogeogr.* **1**, 57–62.

895 Poulton S. W. and Canfield D. E. (2005) Development of a sequential extraction procedure
896 for iron: Implications for iron partitioning in continentally derived particulates. *Chem.*
897 *Geol.* **214**, 209–221.

898 Pye K., Dickson J. A. D., Schiavon N., Coleman M. L. and Cox M. (1990) Formation of
899 siderite-Mg-calcite-iron sulphide concretions in intertidal marsh and sandflat sediments,
900 north Norfolk, England. *Sedimentology* **37**, 325–343.

901 Raiswell R. and Canfield D. E. (2012) The Iron Biogeochemical Cycle Past and Present.
902 *Geochemical Perspect.* **1**, 1–232.

903 Rijken M. (1979) Food and food uptake in Arenicola Marina. *Netherlands J. Sea Res.* **13**,
904 406–421.

905 Robbins J. A., McCall P. L., Berton Fisher J. and Krezoski J. R. (1979) Effect of deposit
906 Feeders on migration of ¹³⁷CS in lake sediments. *Earth Planet. Sci. Lett.* **42**, 277–287.
907 Available at: <https://www.degruyter.com/view/books/9783110490831/9783110490831-001/9783110490831-001.xml>.

909 Sanchez-Cabeza J. A., Ani-Ragolta I. and Masquè P. (2000) Some considerations of the ²¹⁰Pb
910 constant rate of supply (CRS) dating model. *Limnol. Oceanogr.* **45**, 990–995. Available
911 at: <http://doi.wiley.com/10.4319/lo.2000.45.4.0990>.

912 Sanchez-Cabeza J. A. and Ruiz-Fernández A. C. (2012) ²¹⁰Pb sediment radiochronology: An
913 integrated formulation and classification of dating models. *Geochim. Cosmochim. Acta*
914 **82**, 183–200.

915 Slomp C. P., Malschaert J. F. P., Lohse L. and Van Raaphorst W. (1997) Iron and manganese
916 cycling in different sedimentary environments on the North Sea continental margin.
917 *Cont. Shelf Res.* **17**, 1083–1117.

918 Soetaert K., Petzoldt T. and Meysman F. J. R. (2010) marelac: Tools for Aquatic Sciences R
919 package version 2.1.

920 Spivak A. C., Gosselin K., Howard E., Mariotti G., Forbrich I., Stanley R. and Sylva S. P.
921 (2017) Shallow ponds are heterogeneous habitats within a temperate salt marsh
922 ecosystem. *J. Geophys. Res. Biogeosciences* **122**, 1371–1384. Available at:
923 <http://doi.wiley.com/10.1002/2017JG003780> [Accessed March 6, 2018].

924 Spivak A. C., Gosselin K. M. and Sylva S. P. (2018) Shallow ponds are biogeochemically
925 distinct habitats in salt marsh ecosystems. *Limnol. Oceanogr.* **63**, 1622–1642.

926 Swider K. T. and Mackin J. E. (1989) Transformations of sulfur compounds in marsh-flat
927 sediments. *Geochim. Cosmochim. Acta* **53**, 2311–2323.

928 Thamdrup B., Fossing H. and Jorgensen B. B. (1994) Manganese, iron, and sulfur cycling in a
929 coastal marine sediment, Aarhus Bay, Denmark. *Geochim. Cosmochim. Acta* **58**, 5115–
930 5129.

931 Thibault de Chanvalon A., Metzger E., Mouret A., Knoery J., Geslin E. and Meysman F. J. R.
932 (2017) Two dimensional mapping of iron release in marine sediments at submillimetre
933 scale. *Mar. Chem.* **191**, 34–49. Available at:
934 <http://dx.doi.org/10.1016/j.marchem.2016.04.003>.

935 van de Velde S. and Meysman F. J. R. (2016) The influence of bioturbation on iron and
936 sulphur cycling in marine sediments: a model analysis. *Aquat. Geochemistry* **22**, 469–
937 504.

938 van de Velde S., Mills B., Meysman F. J., Lenton T. M. and Poulton S. W. (2018) Early
939 Palaeozoic ocean anoxia and global warming driven by the evolution of shallow

940 burrowing. *Nat. Commun.* **9**, 2554.
941 Welsh D. T. (2003) It's a dirty job but someone has to do it: The role of marine benthic
942 macrofauna in organic matter turnover and nutrient recycling to the water column. *Chem.*
943 *Ecol.* **19**, 321–342. Available at:
944 <http://www.tandfonline.com/doi/abs/10.1080/0275754031000155474>.
945 Widerlund A. and Ingri J. (1996) Redox Cycling of Iron and Manganese in Sediments of the
946 Kalix River Estuary, Northern Sweden. *Aquat. Geochemistry* **2**, 185–201.
947 Wijsman J. W. M., Middelburg J. J. and Heip C. H. R. (2001) Reactive iron in Black Sea
948 Sediments: Implications for iron recycling. *Mar. Geol.* **172**, 167–180.
949

950 **Appendix 1: Diagenetic model formulation**

951 **Biogeochemical Model Formulation**

952 The biogeochemical model description follows the standard approach to describe reactive
953 transport in marine sediment and comprises a conventional early diagenetic model (Boudreau,
954 1997; Berg et al., 2003; Meysman et al., 2003). The core of this reactive transport model
955 consists of a set of mass balance equations of the advection-diffusion-reaction form (Boudreau,
956 1997; Meysman et al., 2005). Adopting the assumption of steady-state compaction, the balance
957 equation for a pore-water solute and solid components becomes (Meysman et al., 2005):

$$\begin{aligned} \phi_F \frac{\partial C_i}{\partial t} &= \frac{\partial}{\partial x} \left[\phi_F D_i \frac{\partial C_i}{\partial x} - \phi_F^\infty v_F C_i \right] + \phi_F \alpha_i (C_i^{OW} - C_i) + \sum_k v_{i,k} R_k \\ \phi_S \frac{\partial S_j}{\partial t} &= \frac{\partial}{\partial x} \left[\phi_S D_B \frac{\partial S_j}{\partial x} - \phi_S^\infty v_S S_j \right] + \sum_k v_{j,k} R_k \end{aligned} \quad [1]$$

959 The quantity C_i represents the concentration of a pore-water compound, C_i^{OW} is the value in
960 the overlying water, ϕ_F denotes the porosity (implemented via an exponentially decreasing
961 depth relation as described below), ϕ_F^∞ is the asymptotic porosity at depth, D_i is the diffusion
962 coefficient, and v_F is the burial velocity of the pore fluids. The solid volume fraction is
963 calculated from porosity ($\phi_S = 1 - \phi_F$) and v_S is the burial velocity of the solids. The
964 concentration S_j of a solid compound is expressed per unit volume of solid sediment. The
965 quantities R_k represent the rates of the biogeochemical reactions (expressed per bulk sediment
966 volume), where $v_{i,k}$ is the stoichiometric coefficient of the i -th species in the k -th reaction.

967 **Transport parameters**

968 The model includes four different transport parameters; (i) molecular diffusion, (ii)
969 downward advection as a consequence of burial, (iii) bio-mixing and (iv) bio-irrigation. The
970 solute flux due to molecular diffusion and advection is described by Fick's first law (Fick,
971 1855),

$$972 \quad J_D = -\phi D_i \frac{\partial C_i}{\partial z} + \phi v C_i \quad [2]$$

973 where the molecular diffusion coefficient D_i^{mol} is first calculated as a function of temperature
974 and salinity using the CRAN:marelac package (Soetaert et al., 2010a) and corrected for

975 tortuosity according to the modified Wiessberg relation of Boudreau (1996), i.e.,
 976 $D_i = D_i^{mol} / (1 - 2 \ln \phi_F)$. The model adopts a constant sediment accumulation rate $F_{sed} = 0.10$
 977 $\text{g cm}^{-2} \text{ yr}^{-1}$, determined from core dating (see main text). An exponential declining porosity
 978 profile was imposed,

$$979 \quad \phi_F = \phi_F^0 + (\phi_F^0 - \phi_F^\infty) e^{-z/x_{att}} \quad [3]$$

980 where ϕ_F^0 is 0.96, ϕ_F^∞ is 0.78 and x_{att} is 9 cm (Fig. A1.1a). A change in porosity also implies
 981 sediment compaction with depth, and different burial velocities for solutes and solids. The
 982 burial velocity of the pore fluid at the end of the integration interval is assumed to be the same
 983 as that of the solid phase, i.e. $v_F = v_S$. The depth-dependent advection velocities were
 984 calculated from the porosity profile, the constant F_{sed} and the burial velocity at the end of the
 985 integration interval using the CRAN:ReacTran package (Soetaert and Meysman, 2012).

986 The presence of bioturbation is modelled as two different extra transport parameters; bio-
 987 mixing and bio-irrigation. Following the conventional description, bio-mixing is modelled as a
 988 diffusive process (Boudreau, 1997; Meysman et al., 2010)

$$989 \quad J_b = -\phi_S D_b \frac{\partial S}{\partial z} \quad [4]$$

990 Benthic fauna require food resources (organic matter) that arrive from the overlying water at
 991 the top of the sediment pile, and thus most of their activity occurs near the sediment-water
 992 interface, and decreases with depth (Boudreau, 1998). The bio-diffusivity coefficient
 993 accordingly follows a sigmoidal depth profile

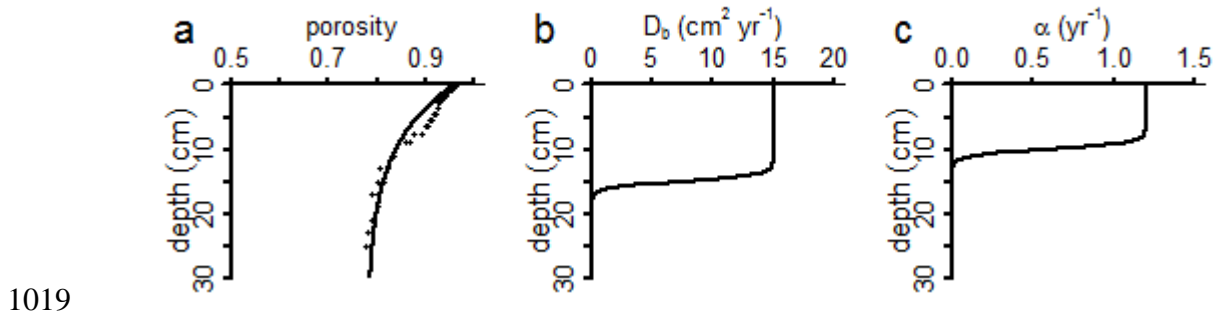
$$994 \quad D_b(z) = D_{b,0} \exp\left(-\frac{(z-x_L)}{0.25x_{bm}}\right) / \left(1 + \exp\left(-\frac{(z-x_L)}{0.25x_{bm}}\right)\right) \quad [5]$$

995 where $D_{b,0}$ is the bio-diffusivity at the sediment-water interface, x_L is the depth of the mixed
 996 layer and x_{bm} is an attenuation coefficient determining the transition zone from mixed to
 997 unmixed sediment horizons. For the unbioturbated site, both $D_{b,0}$ and x_L are set to zero, as no
 998 burrowing fauna was present. For the bioturbated site, x_L was set to 15 cm, which corresponds
 999 to the burrow depth of the two species found at the field site (*Nereis*: 15-20 cm; Esselink and
 1000 Zwarts, 1989; *Arenicola Marina*: 15-18 cm; Rijken, 1979). The high density of burrows
 1001 observed in the sediment suggests high bio-mixing activity, therefore, $D_{b,0}$ was set at 10 cm^2
 1002 yr^{-1} (Fig. A1.1b).

1003 A second requirement for benthic fauna is oxygen. To keep up the supply of oxygen to the
 1004 anoxic sediment layers, burrowing animals can actively flush their burrows. This bio-
 1005 irrigational transport is classically described as a non-local exchange process, where pore-water
 1006 parcels are exchanged with bottom-water parcels (Boudreau, 1984). Bio-irrigation is
 1007 implemented using the same relation as bio-mixing,

$$1008 \quad \alpha(z) = \alpha_0 \exp\left(-\frac{(z - x_{L,irr})}{0.25x_{irr}}\right) \Bigg/ \left(1 + \exp\left(-\frac{(z - x_{L,irr})}{0.25x_{irr}}\right)\right) \quad [6]$$

1009 where α_0 is the bio-irrigation coefficient at the sediment-water interface, $x_{L,irr}$ is the depth of
 1010 the irrigated layer and x_{irr} is an attenuation coefficient determining the transition zone from
 1011 irrigated to un-irrigated sediment horizons. For the unbioturbated sediment, α_0 and $x_{L,irr}$ were
 1012 set to zero, while for the bioturbated sediment $x_{L,irr}$ was set to 10 cm and α_0 was calibrated to
 1013 1.2 yr^{-1} , based on the NH_4^+ profile, assuming that NH_4^+ acts as tracer (Fig. A1.1c). Following
 1014 Meile et al. (2005), we introduce solute-specific irrigation coefficients, to capture the
 1015 differential biogeochemical behaviour of individual pore-water species. For example, the fast
 1016 oxidation kinetics of Fe^{2+} mean that Fe^{2+} generally is not flushed out of the sediment, but is
 1017 oxidised in the worm burrow. The solute specific irrigation coefficients were; $\alpha_{\text{Fe}^{2+}} = 0$, $\alpha_{\text{SO}_4^{2-}}$
 1018 $= 5/6 * \alpha$, $\alpha_{\text{HCO}_3^-} = \alpha$, $\alpha_{\text{HS}^-} = 4/3 * \alpha$, $\alpha_{\text{O}_2} = \alpha$, $\alpha_{\text{NH}_4^+} = \alpha$, $\alpha_{\text{CH}_4} = \alpha$.



1019
 1020 **Figure A 1.1: (a) imposed porosity profile, fitted to the porosity profile of the unbioturbated core from October 2015**
 1021 **(black dots). (b) vertical depth profile of the bio-diffusion coefficient and (c) vertical depth profile of the bio-irrigation**
 1022 **coefficient in the bioturbated scenario.**

1024 **Biogeochemical reaction set**

1025 The reaction set (n=25, note that there are three different fractions of organic matter, and
 1026 two fractions of iron oxides) was chosen to be a parsimonious description of the coupled C, Fe

1027 and S cycles in the sediment of the Blakeney salt marsh (Table A 1.1). To keep the numerical
1028 simulations tractable, manganese and nitrogen cycling were assumed to be of minor
1029 importance, and elemental sulphur was not included. Note that, to match the observed POC
1030 depth profile to the sulphate profile, we assumed that organic carbon had an oxidation state of
1031 -II. In models, it is conventionally assumed that organic carbon has an oxidation state of 0, but
1032 the oxidation state of carbon in organic compounds ranges from -II to +II (Burdige, 2006).
1033 Because we have direct observations of the sedimentation velocity and the mass-% of POC, as
1034 well as direct measurements of the sulphate concentrations, we believe that these parameters
1035 are well constrained. In contrast, we have no data regarding the actual oxidation state of carbon
1036 in organic matter. On average, carbon in marine plankton has an oxidation state of -0.3 to -0.7,
1037 and marine organic matter that has undergone mineralisation has an oxidation state of -0.6 to -
1038 2 (Burdige, 2006). Given the uncertainty of the oxidation state of carbon in organic matter, we
1039 believe that the assumption of a low oxidation state for carbon in this case (-2) is acceptable.

1040 Organic matter consists of three fractions; labile organic matter, which is easily degraded
1041 and has a high decay constant, slow degradable organic matter, which is degraded at an
1042 intermediate rate and refractory organic matter, which is degraded at a slower rate. Each of
1043 these fractions can be degraded by four different mineralisation pathways; aerobic respiration
1044 (AR), dissimilatory iron reduction (DIR), sulphate reduction (SR) and methanogenesis (MG)
1045 (Reactions 1-4; Table A 1.1, note that the same reactions are valid for each of the organic matter
1046 fractions). Denitrification and manganese oxide reduction are not included, as they generally
1047 contribute little to the total mineralisation rate (Thamdrup, 2000), and the low dissolved Mn
1048 concentrations at the field site suggest limited importance of Mn cycling. The classical redox
1049 sequence (Froelich et al., 1979) is implemented via conventional limitation-inhibition
1050 formulations (Table A 1.2; Soetaert et al., 1996). The reduction of organic matter releases
1051 ammonium and bicarbonate in the pore water. Ammonium can adsorb on solid-phase particles
1052 (Mackin and Aller, 1984). The adsorption of ammonium is included as a reversible, linear
1053 adsorption process, where the concentration of adsorbed ion is in equilibrium at all times with
1054 the surrounding pore water, i.e., $[X \equiv NH_4^+] = K_{ads}^{NH_4^+} [NH_4^+]$, where $K_{ads}^{NH_4^+}$ is the dimensionless
1055 adsorption constant (Berg et al., 2003).

1056 Iron oxides are modelled as two separate fractions; fresh iron oxides and aged iron oxides,
1057 where the fresh iron oxide fraction can reduce organic matter and oxidise sulphide, and the aged
1058 iron oxides only reacts with sulphide (Berg et al., 2003). Organic matter mineralisation coupled
1059 to iron oxide reduction released ferrous iron (Fe^{2+}) in the pore water, which can (i) adsorb on

1060 solid-phase particles (Berg et al., 2003), (ii) become re-oxidised by oxygen or (iii) precipitate
1061 as iron sulphide (Table A 1.2). Iron oxide reduction coupled to sulphide oxidation immediately
1062 captures Fe^{2+} as FeS. Sulphate reduction produces free sulphide, which can be (i) re-oxidised
1063 by oxygen, (ii) re-oxidised by iron oxide, (iii) precipitated as FeS, (iv) reaction with FeS to
1064 form FeS_2 (Table A 1.2). When all electron acceptors are depleted, methanogenesis produces
1065 methane, which can be (i) oxidised by oxygen, or (ii) oxidised by sulphate. The kinetic rate
1066 expressions of all re-oxidation processes are described by standard second-order rate laws
1067 (Table A1.2). To simplify the reaction set, FeS is assumed to directly precipitate with sulphide-
1068 mediated iron reduction (Table A 1.1).
1069

Kinetic reactions		
R1	Aerobic respiration	$\{CH_2 \cdot (NH_3)_{1/R_{CN}}\}_{f,s,r} + \frac{3}{2}O_2 \rightarrow HCO_3^- + \frac{1}{R_{CN}}NH_4^+ + \frac{R_{CN}-1}{R_{CN}}H^+$
R2	Dissimilatory Iron reduction	$\{CH_2 \cdot (NH_3)_{1/R_{CN}}\}_{f,s,r} + 6FeOOH_f + \frac{11R_{CN}+1}{R_{CN}}H^+ \rightarrow HCO_3^- + \frac{1}{R_{CN}}NH_4^+ + 6Fe^{2+} + 9H_2O$
R3	Sulphate reduction	$\{CH_2 \cdot (NH_3)_{1/R_{CN}}\}_{f,s,r} + \frac{3}{4}SO_4^{2-} + \frac{4-R_{CN}}{4R_{CN}}H^+ \rightarrow HCO_3^- + \frac{1}{R_{CN}}NH_4^+ + \frac{3}{4}HS^-$
R4	Methanogenesis	$\{CH_2 \cdot (NH_3)_{1/R_{CN}}\}_{f,s,r} + \frac{3}{4}H_2O + \frac{4-R_{CN}}{4R_{CN}}H^+ \rightarrow \frac{1}{4}HCO_3^- + \frac{1}{R_{CN}}NH_4^+ + \frac{3}{4}CH_4$
R5a	Ferrous iron oxidation	$4Fe^{2+} + O_2 + 6H_2O \rightarrow 4FeOOH_f + 8H^+$
R5b	Adsorbed iron oxidation	$4X \equiv Fe^{2+} + O_2 + 6H_2O \rightarrow 4FeOOH_f + 8H^+$
R6	Canonical sulphur oxidation	$HS^- + 2O_2 \rightarrow SO_4^{2-} + H^+$
R7	Sulphide-mediated iron reduction	$9HS^- + 8FeOOH_{f,a} + 7H^+ \rightarrow SO_4^{2-} + 8FeS + 12H_2O$
R8	Iron sulphide oxidation	$FeS + \frac{9}{4}O_2 + \frac{3}{2}H_2O \rightarrow FeOOH_f + SO_4^{2-} + 2H^+$
R9	Pyrite precipitation	$FeS + \frac{1}{4}SO_4^{2-} + \frac{3}{4}HS^- + \frac{5}{4}H^+ \rightarrow FeS_2 + H_2O$
R10	Pyrite oxidation	$FeS_2 + \frac{15}{4}O_2 + \frac{5}{2}H_2O \rightarrow 2SO_4^{2-} + FeOOH_f + 4H^+$
R11	Aerobic methane oxidation	$CH_4 + 2O_2 \rightarrow CO_2 + 2H_2O$
R12	Anaerobic methane oxidation	$CH_4 + SO_4^{2-} + H^+ \rightarrow CO_2 + HS^- + 2H_2O$
R13	Iron oxide aging	$FeOOH_f \rightarrow FeOOH_a$
R14	Ferrous iron sorption	$Fe^{2+} \rightarrow X \equiv Fe^{2+}$
R15	Ammonium sorption	$NH_4^+ \rightarrow X \equiv NH_4^+$

1070 **Table A 1.1:** list of reactions included in the model

1071

1072 **Model parametrisation and boundary conditions**

1073 Our model analysis aimed to explore the impact of bioturbation on the coupled
1074 biogeochemical cycles of C, Fe and S. In the first step, we calibrated our model parameters and
1075 boundary conditions on the bioturbated pond of the Blakeney salt marsh (see below), for the
1076 parameters where no calibration was required, we used literature values (Table A 1.3). The
1077 upper boundary conditions for dissolved constituents was set at fixed concentration, based on
1078 *in situ* measurements. The upper boundary conditions for solid-phase species were set at “fixed
1079 flux”, calibrated on the *in situ* data (see main text). For all species, the lower boundary
1080 condition was set at ‘no gradient’, apart from SO_4^{2-} and HS^- , for which a clear downward
1081 gradient was present. For these species, we set the boundary condition at ‘fixed concentration’.

1082 **Numerical solution**

1083 The model includes 14 state variables; the concentrations of labile organic matter $[\text{CH}_2\text{O}]_f$
1084 , slow degradable organic matter $[\text{CH}_2\text{O}]_s$, refractory organic matter $[\text{CH}_2\text{O}]_r$, dissolved
1085 inorganic carbon $[\text{HCO}_3^-]$, dissolved ammonium $[\text{NH}_4^+]$ oxygen $[\text{O}_2]$, fresh iron oxide
1086 $[\text{FeOOH}]_f$, aged iron oxide $[\text{FeOOH}]_a$, ferrous iron $[\text{Fe}^{2+}]$, sulphate $[\text{SO}_4^{2-}]$, free sulphide
1087 $[\text{H}_2\text{S}]$, iron sulphide $[\text{FeS}]$, pyrite $[\text{FeS}_2]$ and methane $[\text{CH}_4]$. The open-source
1088 programming language R was used to implement a numerical solution procedure for the partial
1089 differential equations, following the procedures of Soetaert and Meysman (2012). The spatial
1090 derivatives within the partial differential equations (Eq. [1]) were expanded over the sediment
1091 grid using finite differences by using the R package CRAN:ReacTran (Soetaert and Meysman,
1092 2012). This sediment grid was generated by dividing the sediment domain (thickness $L = 30$
1093 cm) into 400 sediment layers of equal thickness. The resulting set of ordinary differential
1094 equations was integrated using the stiff equation solver routine ‘vode’ (Brown et al., 1989)
1095 within the package CRAN:deSolve (Soetaert et al., 2010b). All model simulations were run for
1096 a sufficiently long time period (>1000 year) to allow them to reach a steady state.

1097

Kinetic rate expression	
	$R_{\min} = \varphi_S k_{\min} [CH_2O]$
R1	$R = R_{\min} \frac{[O_2]}{[O_2] + K_{O_2}}$
R2	$R = R_{\min} \frac{K_{O_2}}{[O_2] + K_{O_2}} \frac{[FeOOH]}{[FeOOH] + K_{FeOOH}}$
R3	$R = R_{\min} \frac{K_{O_2}}{[O_2] + K_{O_2}} \frac{K_{FeOOH}}{[FeOOH] + K_{FeOOH}} \frac{[SO_4^{2-}]}{[SO_4^{2-}] + K_{SO_4^{2-}}}$
R4	$R = R_{\min} \frac{K_{O_2}}{[O_2] + K_{O_2}} \frac{K_{FeOOH}}{[FeOOH] + K_{FeOOH}} \frac{K_{SO_4^{2-}}}{[SO_4^{2-}] + K_{SO_4^{2-}}}$
R5a	$R = \varphi_F k_{FIO} [Fe^{2+}][O_2]$
R5b	$R = \varphi_S k_{FIO} [X \equiv Fe^{2+}][O_2]$
R6	$R = \varphi_F k_{CSO} [HS^-][O_2]$
R7	$R = \varphi_S k_{SMI} [HS^-][FeOOH]$
R8	$R = \varphi_S k_{ISO} [FeS][O_2]$
R9	$R = \varphi_S k_{PyP} [FeS][HS^-]$
R10	$R = \varphi_S k_{PyO} [FeS_2][O_2]$
R11	$R = \varphi_F k_{AMO} [CH_4][O_2]$
R12	$R = \varphi_F k_{AnMO} [CH_4][SO_4^{2-}]$
R13	$R = \varphi_S k_{IOA} [FeOOH_f]$

1098 **Table A 1.2:** List of kinetic expressions included in the model

1099

1100

ENVIRONMENTAL PARAMETERS	Symbol	Value	Units	Method	References
Temperature	T	10	°C	A	
Salinity	S	32	-	A	
Porosity (surface value)	ϕ_F^0	0.96	-	A	
Porosity (asymptotic at depth)	ϕ_F^∞	0.78	-	A	
Porosity attenuation coefficient	x_ϕ	9	cm	A	
Solid-phase density	ρ_S	2.0	g cm ⁻³	A	
Sediment accumulation rate	F_{sed}	0.10	g cm ² yr ⁻¹	A	
Depth of sediment domain	L	30	cm	-	
BOUNDARY CONDITIONS	Symbol	Value	Units	Method	References
Oxygen bottom water	[O ₂]	0.28	mol m ⁻³	A	
Sulphate bottom water	[SO ₄ ²⁻]	20	mol m ⁻³	A	
DIC bottom water	∑CO ₂	3.9	mol m ⁻³	A	
Ammonium bottom water	[NH ₄ ⁺]	0.01	mol m ⁻³	A	
Ferrous iron bottom water	[Fe ²⁺]	0	mol m ⁻³	A	
Free sulphide bottom water	[HS ⁻]	0	mol m ⁻³	A	
Methane bottom water	[CH ₄]	0	mol m ⁻³	A	
Flux OM fast decaying	F _{OM,F}	17	mmol m ⁻² d ⁻¹	B	
Flux OM slow decaying	F _{OM,S}	14	mmol m ⁻² d ⁻¹	B	
Flux OM refractory	F _{OM,r}	13	mmol m ⁻² d ⁻¹	B	
Flux FeOOH fresh	F _{FeOOH,f}	0.44	mmol m ⁻² d ⁻¹	B	
Flux FeOOH aged	F _{FeOOH,a}	0.44	mmol m ⁻² d ⁻¹	B	
Flux FeS	F _{FeS}	0	mmol m ⁻² d ⁻¹	B	
Flux FeS ₂	F _{FeS2}	0	mmol m ⁻² d ⁻¹	B	

1102 **Table A 1.3:** List of parameters included in the model. Solid-phase concentrations are expressed per unit volume of solid phase.
1103 “Method” refers to the procedure by which parameter values are constrained: A = Measurements, B = model calibration, C=
1104 Literature values. References: [1] Meysman et al., (2003) [2] van de Velde and Meysman (2016), [3] Poulton and Canfield,
1105 (2005) [4] Meysman et al., (2015), [5] Berg et al., 2003.

1106

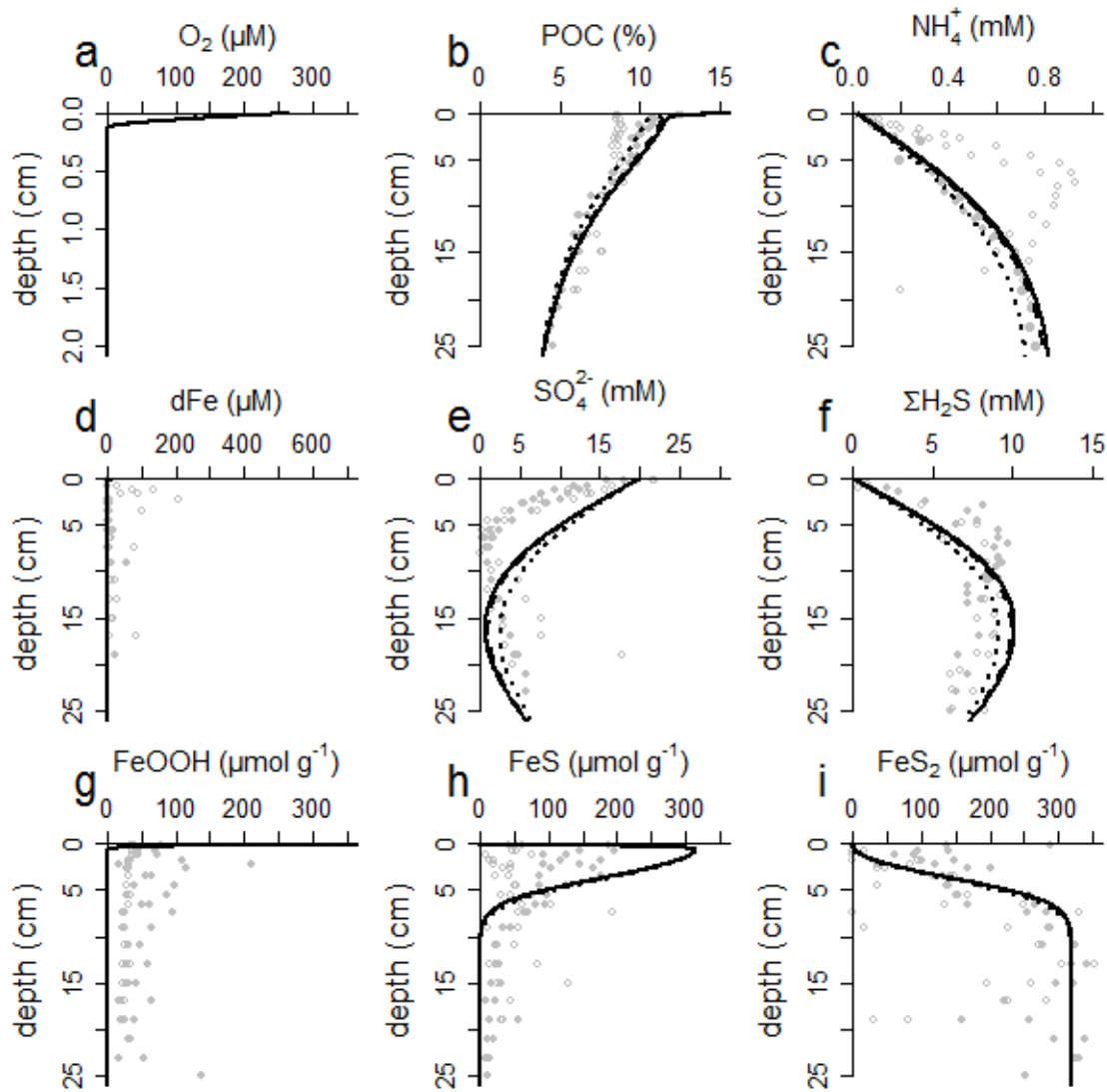
BIOGEOCHEMICAL PARAMETERS	Symbol	Value	Units	Method	References
Mixing depth	L_{mix}	15	cm	B	
Biodiffusion coefficient	D_b	10	cm ² yr ⁻¹	B	
Bio-irrigation coefficient	α_0	1.2	yr ⁻¹	B	
Mineralization constant fast	k_f	10	yr ⁻¹	B	
Mineralization constant slow	k_s	0.04	yr ⁻¹	B	
Mineralization constant refractory	k_r	0.005	yr ⁻¹	B	
Oxygen saturation constant	K_{O_2}	0.008	mol m ⁻³	C	[1]
FeOOH saturation constant	K_{FeOOH}	0.4	μmol g ⁻¹	C	[2]
Sulphate saturation constant	$K_{SO_4^{2-}}$	0.9	mol m ⁻³	C	[1]
C:N ratio organic matter	$C_{org} : N_{org}$	35	-	B	
Ferrous iron oxidation	k_{FIO}	10 ⁺⁷	μmol cm ³ yr ⁻¹	C	[1]
Canonical sulphur oxidation	k_{CSO}	10 ⁺⁷	μmol cm ³ yr ⁻¹	C	[1]
Sulphide-mediated iron reduction	$(k_{SMI})_f$	494	μmol cm ³ yr ⁻¹	C	[3]
Sulphide-mediated iron reduction	$(k_{SMI})_a$	3.6	μmol cm ³ yr ⁻¹	C	[3]
Iron sulphide precipitation	k_{ISP}	10 ⁺⁴	μmol cm ³ yr ⁻¹	C	[4]
Iron sulphide oxidation	k_{ISO}	10 ⁺⁷	μmol cm ³ yr ⁻¹	C	[4]
Pyrite precipitation	k_{PyP}	0.725	μmol cm ³ yr ⁻¹	B	
Pyrite oxidation	k_{PyO}	9.47	μmol cm ³ yr ⁻¹	C	[5]
Aerobic methane oxidation	k_{AMO}	10 ⁺⁴	μmol cm ³ yr ⁻¹	C	[1]
Anaerobic methane oxidation	k_{AnMO}	10	μmol cm ³ yr ⁻¹	C	[1]
Iron oxide ageing	k_{IOA}	0.57	yr ⁻¹	C	[5]
Equilibrium constant ferrous iron sorption	$K_{ads}^{Fe^{2+}}$	696	-	C	[5]
Equilibrium constant ammonium sorption	$K_{ads}^{NH_4^+}$	3.84	-	C	[5]

1107 **Table A 1.3** continued

1108

1109 **Modelled scenarios**

1110 In a first step, the model was parameterised to fit the depth profiles in the unbioturbated ponds
1111 (Fig. A 1.2). When possible, the model parameters and boundary conditions (concentrations
1112 and fluxes) were taken from *in situ* measurements. Other parameters were either calibrated on
1113 the depth profiles of the pore-water and solid-phase constituents of the unbioturbated sediment
1114 or taken from literature values (Table A 1.3).



1115

1116 **Figure A 1.2:** Sensitivity test of the unbioturbated model. Full line = unbioturbated baseline ('U'), Dashed line = aerobic
 1117 stimulation ('U + AS'), Dotted line = self-priming ('U + SP').

1118

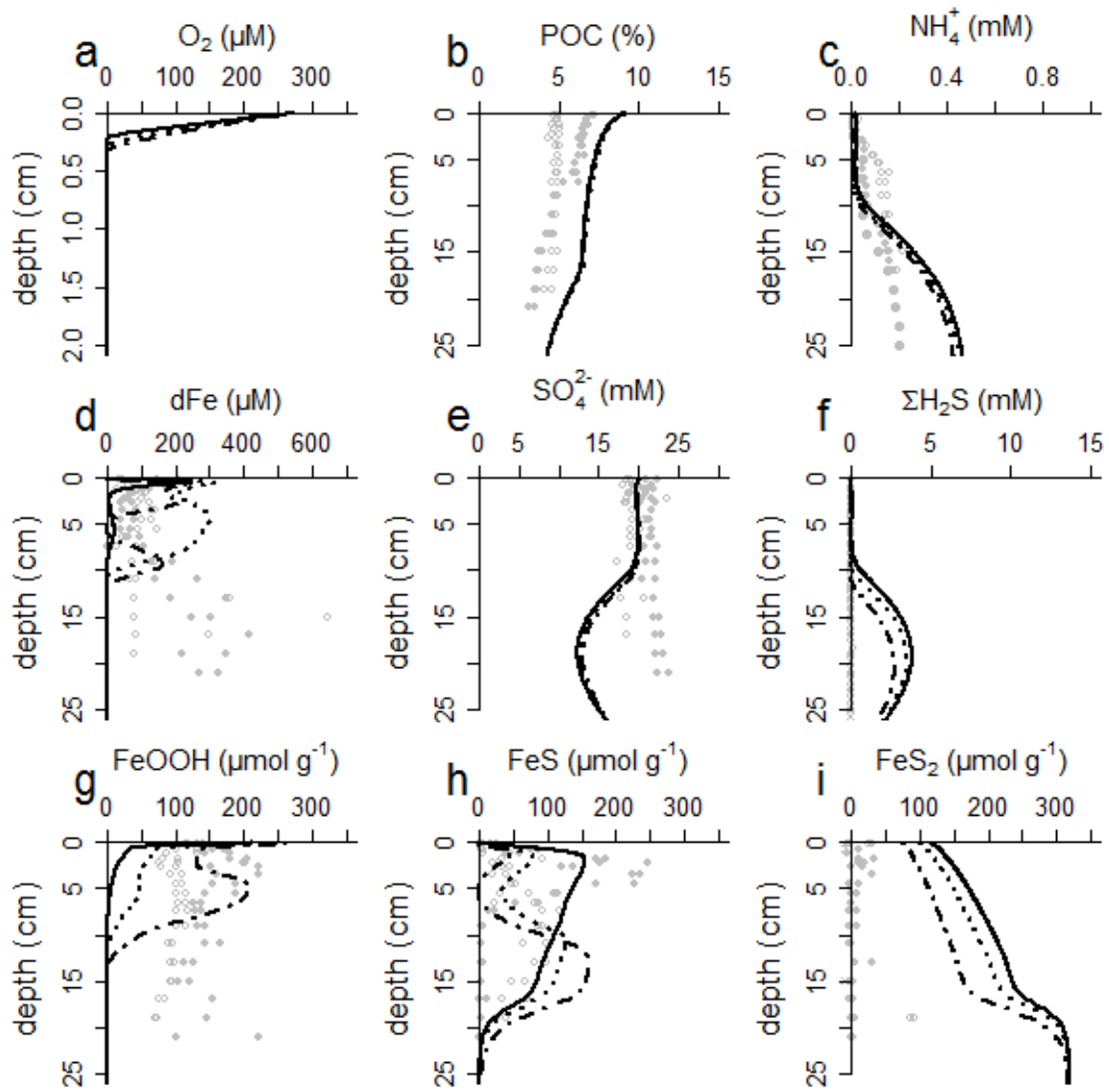
1119 The sediment in the unbioturbated ponds was subsequently modelled using the same
 1120 parameter set, but extended with extra bioturbation parameters. We explored the effect of
 1121 bioturbating fauna on the sedimentary cycles of C, Fe and S by running three scenarios; (i)
 1122 'Bioturbation' (scenario 'B'), (ii) 'bioturbation + aerobic stimulation' (scenario 'B + AS') and
 1123 (iii) 'bioturbation + self-priming' (scenario 'B + SP'). In the first scenario ('B'), bioturbation
 1124 introduces extra transport via bio-mixing ($D_{b,0} = 10 \text{ cm}^2 \text{ yr}^{-1}$ over 15 cm) and bio-irrigation (
 1125 $\alpha_0 = 1.2 \text{ yr}^{-1}$ over 10 cm) – see Fig. A 1.1. In the second scenario ('B + AS'), bioturbation
 1126 introduces extra transport, but we additionally assume that aerobic respiration is more efficient

1127 at breaking down the refractory organic matter fractions (Kristensen, 2000). Non-labile organic
 1128 matter is broken down 10 times faster by O₂ ($k_{\min, O_2} = 10k_{\min}$). In the third scenario ('B + SP'),
 1129 bioturbation introduces extra transport, and we assume that the breakdown of the non-labile
 1130 organic matter fractions is stimulated in the presence of labile organic matter (Canfield, 1994;
 1131 Burdige, 2007). For this, the kinetic constant of the other organic matter fractions is made
 1132 dependent on the concentration of fast degradable organic matter ($[OC_f]$);
 1133 $k_{\min} = k_{\min,0} + k_{\min,0} f_{\text{priming}} (1 - e^{-[OC_f]/[OC_f]_{\text{ref}}})$, where $k_{\min,0}$ is the kinetic constant without self-
 1134 priming, f_{priming} is the priming factor ($f_{\text{priming}} = 9$) and $[OC_f]_{\text{ref}}$ is a reference concentration (
 1135 $[OC_f]_{\text{ref}} = 100 \mu\text{mol cm}^{-3}$). The priming factors were derived from model fitting.

1136 The results for all scenarios are shown in Figs A 1.3 – 1.6. None of the tested bioturbation
 1137 scenarios perfectly match the observed concentration profiles (Figs A 1.3 – 1.6). This could be
 1138 due to uncertainty in the parameterisation of bioturbation transport, as the high variability in
 1139 the ²¹⁰Pb data did not allow us to constrain a mixing intensity or depth (section 3.2 in main
 1140 text). Additionally, we did not have any direct measurements of the bio-irrigation rate.
 1141 Furthermore, modelling bio-irrigation in a 1-D diagenetic model remains challenging. For
 1142 example, whereas the non-local exchange term that we use in our diagenetic model is valid in
 1143 general (Boudreau, 1984), its parameterisation is solute-dependent, and can differ between
 1144 situations (Meile et al., 2005). Furthermore, the Fe-S interactions during early diagenesis are
 1145 very complex, and involve a number of intermediate reaction steps (Jørgensen et al., 2019) that
 1146 are not represented in our model because of numerical efficiency and lack of proper rate
 1147 constraints.

1148 Nevertheless, the model simulation with priming ("scenario B + SP") and high bio-irrigation
 1149 (1.2 yr^{-1}) does capture the important trends in the depth profiles (dash-dotted line in Fig. A 1.6),
 1150 and so we believe the modelled reaction rates provide a representative picture of the natural
 1151 situation. As it happens, the simulated sulphate reduction rate ($14.7 \text{ mmol S m}^{-2} \text{ d}^{-1}$) agrees with
 1152 the depth-integrated sulphate reduction rate of $14.2 \text{ mmol S m}^{-2} \text{ d}^{-1}$ previously measured in
 1153 slurry incubation experiments using bioturbated salt marsh sediments from Blakeney (Mills et
 1154 al., 2016).

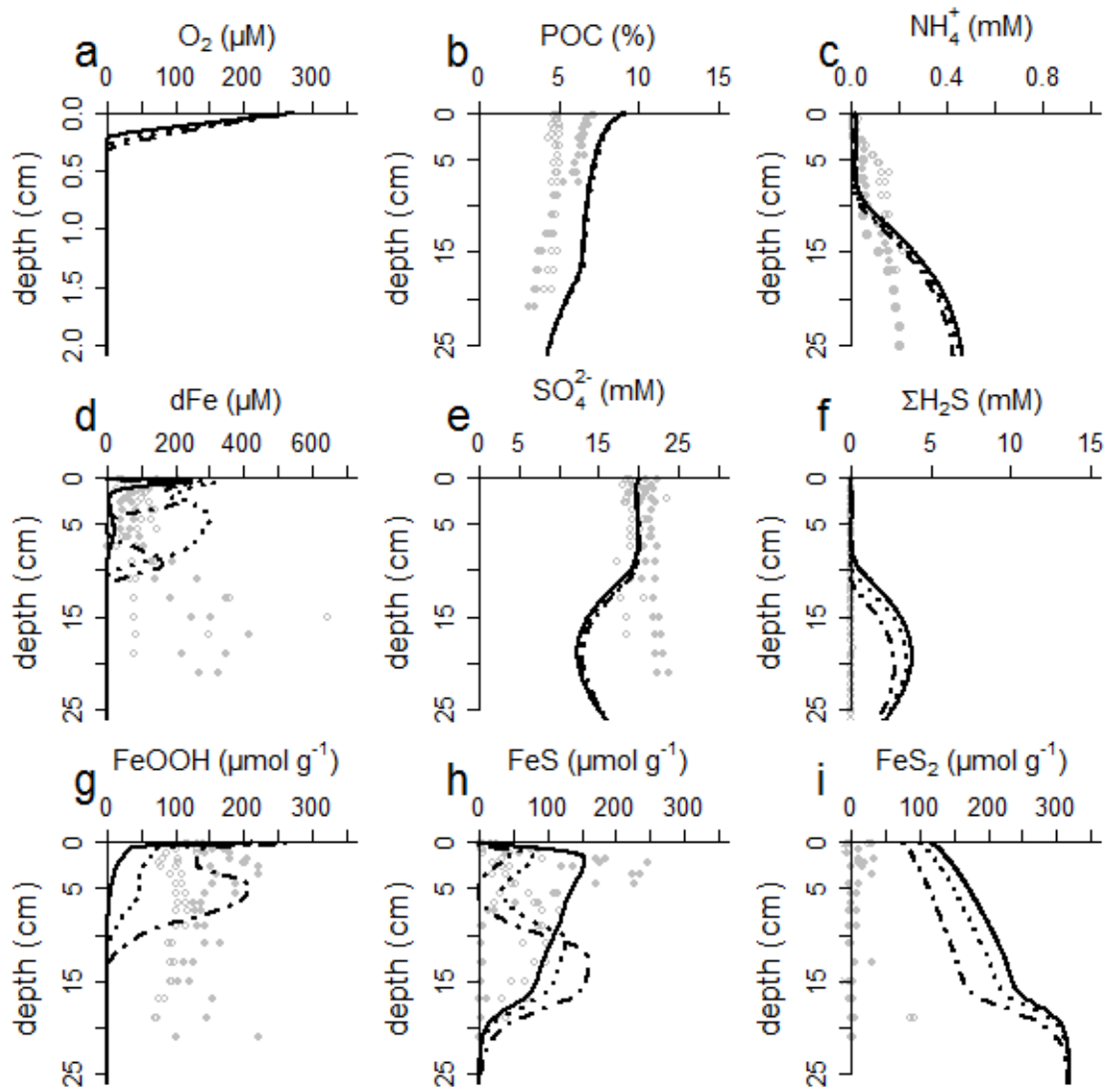
1155



1156

1157 **Figure A 1.3:** Sensitivity test of the bioturbated baseline model (scenario 'B') with higher bio-irrigation. Full line $\alpha_0 = 0.5 \text{ yr}^{-1}$

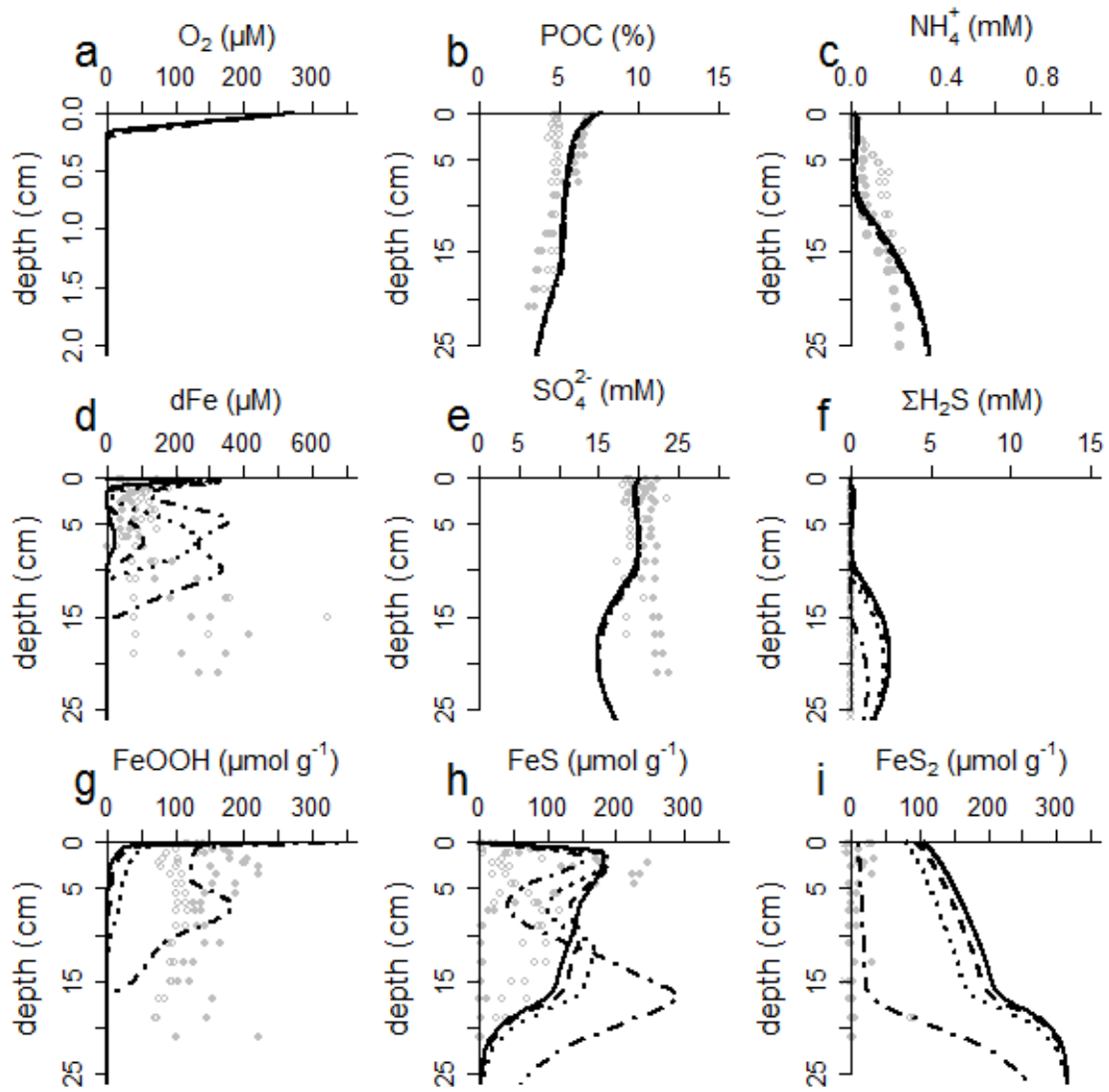
1158 ¹, Dashed line $\alpha_0 = 0.75 \text{ yr}^{-1}$, Dotted line $\alpha_0 = 1 \text{ yr}^{-1}$, Dash-dotted line $\alpha_0 = 1.2 \text{ yr}^{-1}$



1159

1160 **Figure A 1.4:** Sensitivity test of the bioturbated aerobic stimulation model (scenario 'B + AS') with higher bio-irrigation.

1161 Full line $\alpha_0 = 0.5 \text{ yr}^{-1}$, Dashed line $\alpha_0 = 0.75 \text{ yr}^{-1}$, Dotted line $\alpha_0 = 1 \text{ yr}^{-1}$, Dash-dotted line $\alpha_0 = 1.2 \text{ yr}^{-1}$



1162

1163 **Figure A 1.5:** Sensitivity test of the bioturbated self-priming model (scenario 'B + SP') with higher bio-irrigation. Full line

1164 $\alpha_0 = 0.5 \text{ yr}^{-1}$, Dashed line $\alpha_0 = 0.75 \text{ yr}^{-1}$, Dotted line $\alpha_0 = 1 \text{ yr}^{-1}$, Dash-dotted line $\alpha_0 = 1.2 \text{ yr}^{-1}$

1165

1166

1167 **Appendix 2: Organic matter balance**

1168 **Estimation of organic matter mineralisation rate**

1169 To examine the organic carbon balance in the sediment, we can write a simplified mass
1170 balance for POC as

$$1171 \quad L \frac{dC}{dt} = (J_{input} - J_{burial}) - R_{min} \quad [7]$$

1172 In this, L is thickness of the sediment domain that is considered, J_{input} is the input of organic
1173 carbon at the sediment-water interface, J_{burial} is the burial flux of organic carbon and R_{min} is
1174 the depth-integrated mineralization rate of organic carbon. At steady state, the POC balance is
1175 given by

$$1176 \quad R_{min} = J_{input} - J_{burial} \quad [8]$$

1177 We further detail this POC budget for the unbioturbated sediment using the POC depth
1178 profile and diffusive fluxes of solutes, as estimated in the previous section. For the bioturbated
1179 sediment, this cannot be done, as the presence of bio-irrigation and bio-mixing implies that
1180 solute fluxes are not exclusively governed by molecular diffusion and that solid-phase transport
1181 is not only driven by sedimentation.

1182 We can estimate the mineralisation rate R_{min} in the unbioturbated pond in 4 alternative ways
1183 (based on particulate organic carbon, ammonium, sulphide or sulphate depth profiles).
1184 Foremost, in an unbioturbated sediment, where solid-phase transport is only governed by
1185 downward advection of accumulating sediment, the flux at any given depth horizon is given by
1186 $J_x = J_s C_x$, where C_x is the concentration of a given solid phase component (this relation
1187 assumes steady-state compaction; Meysman et al., 2005). If we apply this to POC, the input of
1188 organic carbon at the sediment-water interface for the unbioturbated pond is $26 \pm 9 \text{ mmol C m}^{-2}$
1189 d^{-1} in October 2015 and $18 \pm 6 \text{ mmol C m}^{-2} \text{ d}^{-1}$ in August 2016 (Table 2 in main text).
1190 Similarly, the burial flux of POC becomes $10 \pm 3 \text{ mmol C m}^{-2} \text{ d}^{-1}$ in October 2015 and 12 ± 4
1191 $\text{mmol C m}^{-2} \text{ d}^{-1}$ in August 2016 (see main text). The mineralisation rate R_{min} can then be
1192 estimated as the difference between both quantities, as $16 \pm 9 \text{ mmol C m}^{-2} \text{ d}^{-1}$ in October 2015
1193 and $6 \pm 7 \text{ mmol C m}^{-2} \text{ d}^{-1}$ in August 2016. The variation between ponds is likely caused by local
1194 differences in organic matter delivery, or spatial heterogeneity within the ponds.

1195 Alternatively, the mineralisation rate can be estimated from the ammonium production in
1196 the sediment. If we assume that all organic nitrogen is released by mineralisation as NH_4^+ , and
1197 there is no significant oxidation of ammonium (e.g. through nitrification or anammox), the

1198 mineralisation rate can be estimated as

$$1199 \quad R_{\min} = -\left(\frac{C_{org}}{N_{org}}\right) (J_{diff,SWI}^{NH_4^+} - J_{diff,deep}^{NH_4^+}) \quad [9]$$

1200 This leads to an R_{\min} in the unbioturbated pond of $5.8 \pm 0.5 \text{ mmol C m}^{-2} \text{ d}^{-2}$ for October 2015
1201 and $25 \pm 4 \text{ mmol C m}^{-2} \text{ d}^{-2}$ for August.

1202 Thirdly, in unbioturbated sediments with a shallow oxygen penetration depth, most organic
1203 matter is mineralised via sulphate reduction. Accordingly, we can approximate R_{\min} as

$$1204 \quad R_{\min} = -\frac{4}{3} (J_{H_2S,diff,SWI} - J_{H_2S,diff,deep} - J_{S,burial}) \quad [10]$$

1205 In this, $J_{S,burial}$ represents the burial of solid-phase sulphur (iron sulphides and elemental
1206 sulphur) at depth and $4/3$ represents the stoichiometric coefficient for sulphate reduction (4
1207 moles of carbon oxidised per 3 moles of sulphate reduced, which is valid if carbon in organic
1208 matter has an oxidation state of -II; see Appendix 1). This leads to an R_{\min} of $28.7 \pm 0.3 \text{ mmol}$
1209 $\text{C m}^{-2} \text{ d}^{-1}$ in October 2015 and $24.7 \pm 0.3 \text{ mmol C m}^{-2} \text{ d}^{-1}$ in August 2016. In a similar way, R_{\min}
1210 can be calculated using the sulphate uptake of the sediment

$$1211 \quad R_{\min} = \frac{4}{3} (J_{SO_4^{2-},diff,SWI} - J_{SO_4^{2-},diff,deep}) \quad [11]$$

1212 which equals $21.3 \text{ mmol C m}^{-2} \text{ d}^{-1}$ in October 2015 and $33.5 \text{ mmol C m}^{-2} \text{ d}^{-1}$ in August,
1213 remarkably close to the estimate based on the sulphide balance, which suggests that the sulphur
1214 cycle is close to steady state.

1215 It is quite likely that the POC profile underestimates the true mineralisation rate, due to the
1216 coarse core slicing. We actually integrate the upper 0.5 cm of the sediment core, and thus likely
1217 underestimate the true POC flux at the SWI. Additionally, the solid phase is prone to spatial
1218 heterogeneity, as solid-phase particles cannot diffuse like dissolved species. Therefore, we
1219 focus on the mass balance made using the dissolved species. The nitrogen approach estimates
1220 a mineralisation rate that is about half of the sulphur approach. This can be because the bulk
1221 C:N ratio we use does not adequately represent that of the organic matter being mineralised, or
1222 because there is an ammonium sink we have not identified. Inversely, we could be
1223 overestimating the mineralisation rate estimated via the sulphur balance because we do not
1224 know the actual oxidation state of the carbon in organic matter, although that is quite unlikely,
1225 since we already assumed -II, which is the lowest value reported for marine sediments so far
1226 (Burdige, 2006). Given the uncertainty that is associated with both the nitrogen and sulphur
1227 approach, we will use the estimates as a range ($5.8 < R_{\min} < 33.5 \text{ mmol C m}^{-2} \text{ d}^{-1}$) for the rest of
1228 the discussion.

1229 With the R_{\min} estimated, we can calculate the actual organic matter influx in the
 1230 unbioturbated pond as $12.8 < J_{\text{POC,in}} < 46.5 \text{ mmol C m}^{-2} \text{ d}^{-1}$ for October 2015 and $13.8 < J_{\text{POC,in}}$
 1231 $< 49.5 \text{ mmol C m}^{-2} \text{ d}^{-1}$ for August 2016.

1232

1233 **Organic carbon mass budget**

1234 We can rewrite equation [7] as

$$1235 \quad L \frac{d\hat{C}}{dt} = (J_{\text{input}} - v_{\text{sed}} \hat{C}) - k \hat{C} L \quad [12]$$

1236 where concentration $\hat{C} = (1 - \phi_{\text{AVG}}) \rho_s C$ is the bulk volumetric POC where ϕ_{AVG} is the average
 1237 porosity and ρ_s is the solid-phase density in the sediment domain. At steady state ($d\hat{C}/dt = 0$
 1238), one obtains a simple relation for the key factors that control the magnitude of the mean POC

$$1239 \quad \hat{C} = \frac{J_{\text{input}}}{(kL + v_{\text{sed}})} \quad [13]$$

1240 where the sedimentation velocity v_{sed} is 0.3 cm yr^{-1} , and similar in both the bioturbated and
 1241 unbioturbated ponds (see main text). Hence, the factors that explain the difference in the mean
 1242 POC concentration are either that the organic input J_{input} is lower in the bioturbated ponds, or
 1243 that the intrinsic mineralisation rate k is higher in the bioturbated ponds.

1244 The mean POC concentration is $\sim 37\%$ higher in the unbioturbated ponds ($5.1 \pm 0.9\%$ in the
 1245 bioturbated ponds versus $7 \pm 2\%$ in the unbioturbated pond). If J_{input} is the only factor affecting
 1246 the mean POC concentration, then the POC input also has to be 37% lower in the bioturbated
 1247 ponds, since

$$1248 \quad \frac{\hat{C}_{\text{unb}}}{\hat{C}_{\text{biot}}} = \frac{J_{\text{input,unb}}}{(kL + v_{\text{sed}})} \bigg/ \frac{J_{\text{input,biot}}}{(kL + v_{\text{sed}})} = \frac{J_{\text{input,unb}}}{J_{\text{input,biot}}} \quad [14]$$

1249 and thus

$$1250 \quad \frac{\hat{C}_{\text{unb}}}{\hat{C}_{\text{biot}}} = 1.37 = \frac{J_{\text{input,unb}}}{J_{\text{input,biot}}} \quad [15]$$

1251 or

$$1252 \quad J_{\text{input,unb}} = 1.37 J_{\text{input,biot}} \quad [16]$$

1253 Inversely, if the intrinsic mineralisation rate k is the only factor affecting

$$1254 \quad \frac{\hat{C}_{\text{unb}}}{\hat{C}_{\text{biot}}} = \frac{J_{\text{input}}}{(k_{\text{unb}}L + v_{\text{sed}})} \bigg/ \frac{J_{\text{input}}}{(k_{\text{biot}}L + v_{\text{sed}})} = \frac{k_{\text{biot}}L + v_{\text{sed}}}{k_{\text{unb}}L + v_{\text{sed}}} \quad [17]$$

1255 and

$$1256 \quad \frac{\hat{C}_{unb}}{\hat{C}_{biot}} = 1.37 = \frac{k_{biot}L + v_{sed}}{k_{unb}L + v_{sed}} \quad [18]$$

1257 then

$$1258 \quad k_{biot}L + v_{sed} = 1.37k_{unb}L + 1.37v_{sed} \quad [19]$$

1259 and

$$1260 \quad k_{biot} = 1.37k_{unb} + 0.37\frac{v_{sed}}{L} \quad [20]$$

1261 We can estimate the difference in mineralisation rate by using our estimate for the carbon J_{input}
1262 , derived above (13-50 mmol m⁻² d⁻¹), and the calculated burial rate in both pond types (see
1263 main text). The POC burial rate in the unbioturbated pond is 7-16 mmol m⁻² d⁻¹, and 5-12 mmol
1264 m⁻² d⁻¹ in the bioturbated ponds. Assuming that J_{input} is the same, the total mineralisation in the
1265 unbioturbated pond is 6-34 mmol m⁻² d⁻¹, and 8-38 mmol m⁻² d⁻¹ in the bioturbated pond. This
1266 means that the mineralisation in the bioturbated pond is increased by 12 – 33 %.

1267

1268 **Appendix 3: Extra tables**

1269

Fraction	Extraction solution	Extraction time	Ref.
Fe _{carb}	1 M sodium acetate, buffered to pH 4.5 with acetic acid Solvent: milli-Q	24h	(Poulton and Canfield, 2005)
Fe _{ox1}	1 M hydroxylamine hydrochloride Solvent: 25 % v/v acetic acid – milli-Q	24h	(Poulton and Canfield, 2005)
Fe _{ox2}	50 g L ⁻¹ sodium dithionite Solvent: 25 % v/v acetic acid – milli-Q	2h	(Poulton and Canfield, 2005)
Fe _{mag}	0.2 M ammonium oxalate + 0.17 M oxalic acid Solvent: milli-Q	2h	(Poulton and Canfield, 2005)
Fe _{AVS} AVS	6 M HCl Solvent: milli-Q	40 min.	(Kallmeyer et al., 2004) (Canfield et al., 1986) (Cornwell and Morse, 1987)
Fe _{CRS} CRS	N,N di-methyl formamide Chromium solution: 125 g CrCl ₃ .6H ₂ O + 21 mL 37% HCl, bubbled for 20 min. with activated Zinc granules Solvent: milli-Q	40 min.	(Kallmeyer et al., 2004) (Canfield et al., 1986) (Cornwell and Morse, 1987)
S ⁰	Methanol	Overnight	(Kamyshny et al., 2009)

1270 **Table A 1:** Summary of all employed extraction solutions and times in the solid-phase speciation of iron and sulphur. See
 1271 main text for details

1272

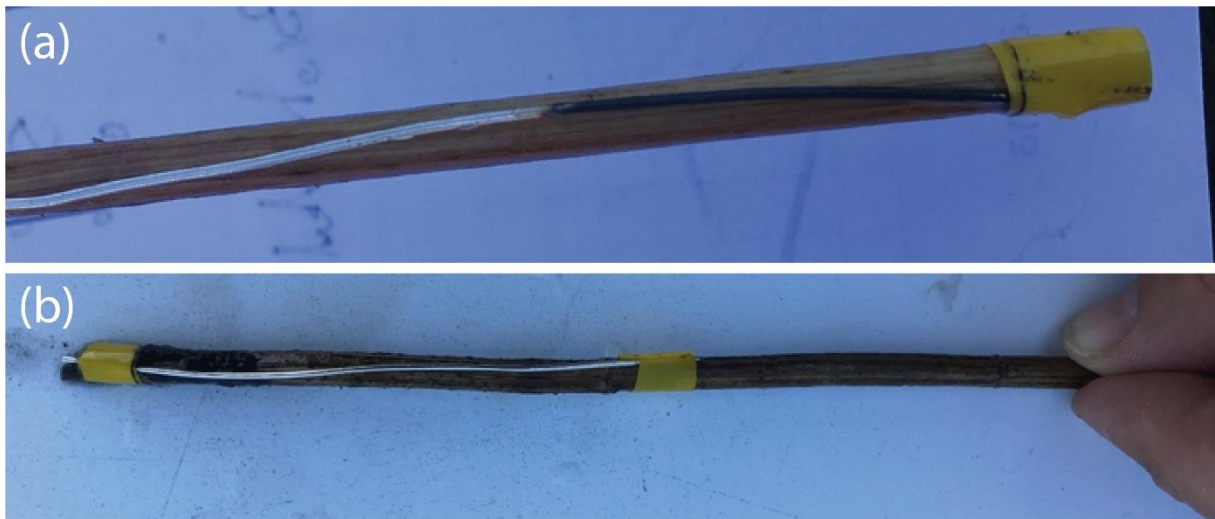
Parameter	Symbol	Unit	Value	
			<i>Unbioturbated</i>	<i>Bioturbated</i>
sediment accumulation rate (SAR)	v	cm yr ⁻¹	0.3 ± 0.1	n.d.
average solid-phase density	$\rho_{solid,av}$	g cm ⁻³	2.2 ± 0.2	2.1 ± 0.2
average porosity	ϕ_{AVG}	-	0.88 ± 0.06	0.79 ± 0.09
sediment flux based on ²¹⁰Pb profile	J_s	kg m⁻² yr⁻¹	0.8 ± 0.2	n.d.
Depth of ¹³⁷ Cs peak	L	cm	15	11
Porosity at sediment-water interface	$\phi_{x=0cm}$	-	0.96	0.92
Porosity at depth L	$\phi_{x=L}$	-	0.81	0.73
sediment flux based on ¹³⁷Cs profile	J_s	kg m⁻² yr⁻¹	0.91 ± 0.08	0.86 ± 0.08

1273 **Table A 2:** Parameters used in the calculations of the sediment flux.

1274

1275 **Appendix 4: Extra Figures**

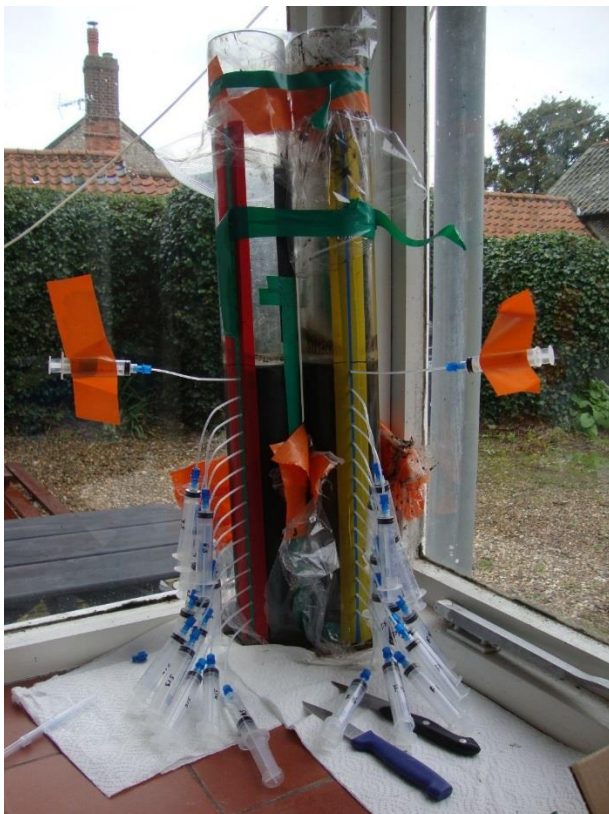
1276



1277

1278 **Figure A 1:** (a) Picture of silver wire from a non-bioturbated pond. (b) Picture of silver wire from a bioturbated pond. The
1279 black colour is evidence for the presence of pore-water sulphide.

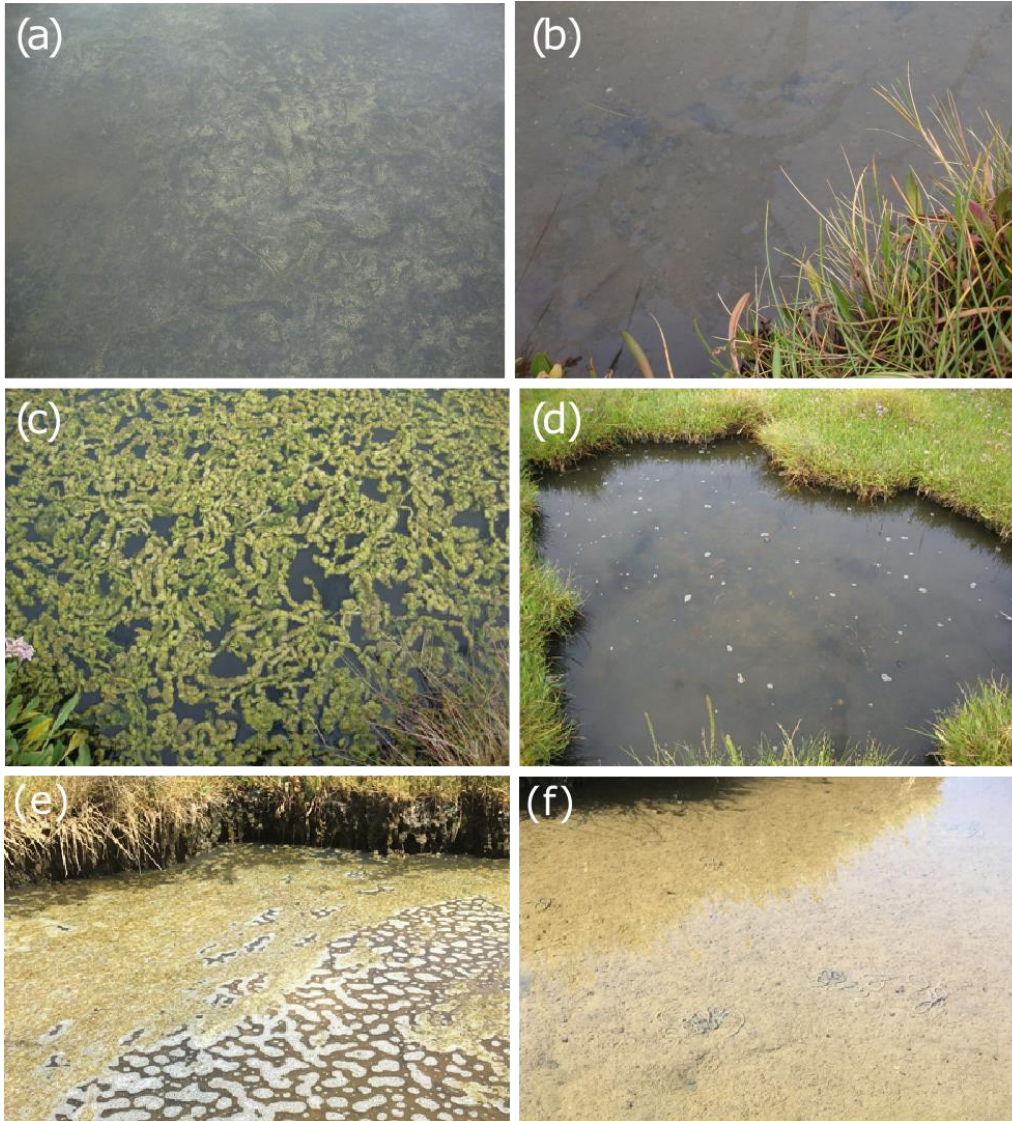
1280



1281

1282 **Figure A 2:** Picture of the rhizon extraction set-up.

1283



1284

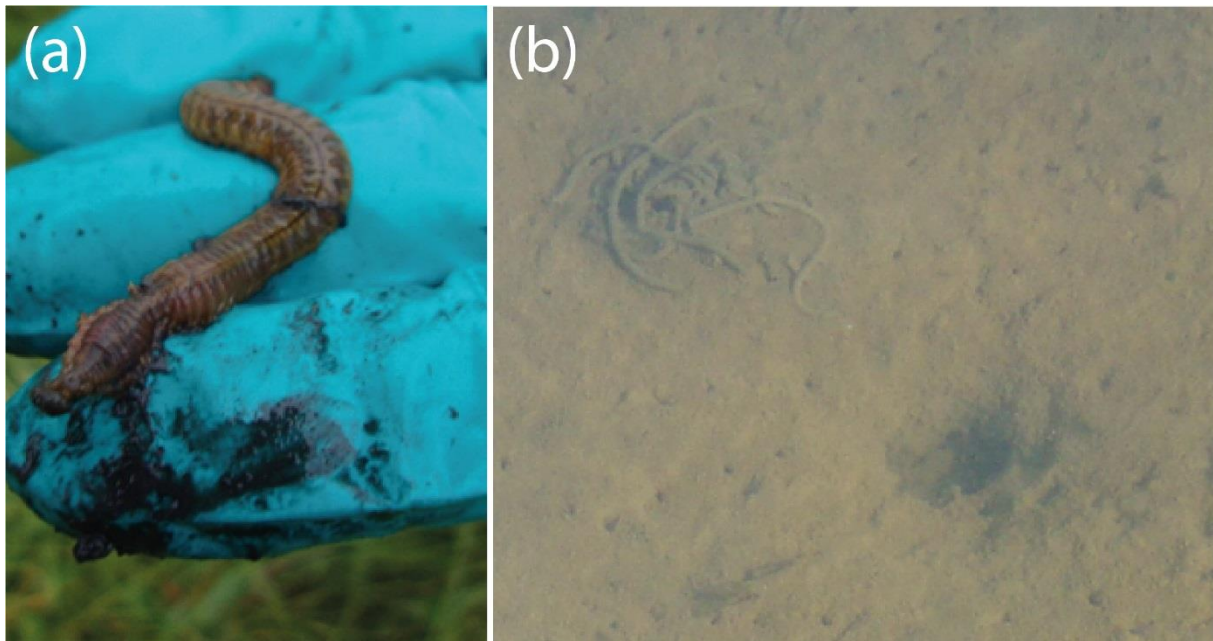
1285

1286

1287

Figure A 3: (a) Picture of an unbioturbated pond in October 2015. (b) Picture of a bioturbated pond in October 2015. (c) Picture of an unbioturbated pond in August 2016. (d) Picture of a bioturbated pond in August 2016. (e) Picture of an unbioturbated pond in August 2018. (f) Picture of a bioturbated pond in August 2018.

1288
1291
1292

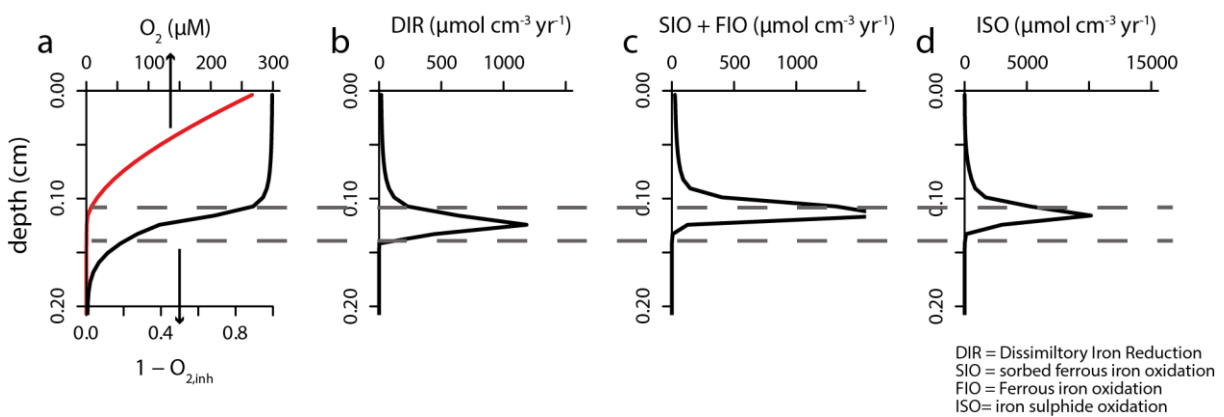


1293

1294 **Figure A 4:** (a) Picture of *Nereis* spp. found at the field site. (b) Visual evidence of the presence of *Arenicola* spp.

1295

1296



1297

1298 **Figure A 5:** Reaction rates associated with the cryptic iron cycle (see main text).

1299

1300

1301

1302